Additive Manufacturing 115 (2026) 105056

Contents lists available at ScienceDirect

Additive Manufacturing

journal homepage: www.elsevier.com/locate/addma

Research paper

A framework for process anomaly detection in 3D concrete printing

Abdallah Kamhawi [a,1], Yuxin Lin [a,1], Christopher Watson [b,*,1], Kira Barton [b,c], Mania Aghaei Meibodi [a]

[a] Taubman College of Architecture and Urban Planning, University of Michigan, Ann Arbor, MI 48109, USA
[b] Robotics Department, University of Michigan, Ann Arbor, MI 48109, USA
[c] Mechanical Engineering Department, University of Michigan, Ann Arbor, MI 48109, USA

ARTICLE INFO

Dataset link: https://doi.org/10.5281/zenodo.17308420

Keywords:
3D concrete printing
Process anomaly detection
Heterogeneous sensing
Real-time monitoring
Signal feature characterization

ABSTRACT

Extrusion-based 3D concrete printing offers a transformative opportunity for waste-free fabrication of complex and materially optimized building components. However, the current reliance on manual observation and ad-hoc parameter tuning introduces significant variability into the process and limits the scalability of 3D concrete printing. Existing systems offer no predictive insight into failure events and remain dependent on trial-and-error methods, resulting in increased material consumption, higher costs, and prolonged production times. To address this, the paper introduces a comprehensive framework for process anomaly detection tailored to two-component extrusion-based 3D concrete printing systems. The proposed framework integrates systematic sensor instrumentation, heterogeneous data acquisition, and signal feature characterization to enable real-time monitoring of system health. Non-destructive sensors are deployed to measure environmental conditions, slurry pumpability, hydration behavior, and workability. Collected signals are analyzed using a suite of processing techniques — including frequency analysis, amplitude envelope detection, curve fitting, and magnitude deviation analysis — to extract critical features indicative of emerging anomalies. The methodology presented in this paper establishes a generalizable framework for anomaly detection, using data collected from physical experiments, where the specific metric values derived from the data are tied to the feedstock used in this study for validation. The paper results demonstrate the ability of the proposed methods to detect failure modes — such as pump clogging, material segregation, and two-component mixing head clogging — ahead of human operator detection. These findings confirm the viability of the proposed framework for anomaly detection.

1. Introduction

1.1. Challenges and complexities in extrusion-based 3D concrete printing

Extrusion-based 3D concrete printing (3DCP) with robotic arm implements represents one prominent subset of 3DCP with the potential to advance the concrete construction industry by enabling rapid waste-free production of complex, materially optimized building components [1–9]. However, a significant challenge is that codes, design rules, and quality control procedures established from conventional concrete casting cannot be directly transferred to 3DCP, resulting in the lack of a standardized manufacturing framework. Consequently, current 3DCP applications are unable to achieve consistent and reproducible outcomes and remain dominated by ad hoc, trial-and-error methods, relying heavily on human heuristics. This not only increases material consumption and costs, but also prolongs production times [10–14].

Compared to conventional concrete casting, 3DCP has a unique manufacturing process chain that requires the coexistence of several conflicting material characteristics, in which concrete must behave simultaneously as a pumpable slurry and a load-bearing solid [15–18]. To ensure successful deposition, the concrete must be fluid enough for smooth pumping and extrusion while rapidly developing strength and stiffness after deposition to retain its shape, which ensures effective buildability and prevents premature failure of the construct [2,19]. However, this transition cannot be immediate, as the extruded concrete must retain adequate workability to ensure proper adhesion between layers and prevent the formation of cold joints [20,21]. Meeting these competing demands requires meticulous control over the fabrication parameters and the non-Newtonian slurry properties of concrete [4,22–

* Corresponding author.
E-mail address: cjwattz@umich.edu (C. Watson).
[1] These authors contributed equally to this work.

https://doi.org/10.1016/j.addma.2025.105056
Received 21 July 2025; Received in revised form 1 December 2025; Accepted 15 December 2025
Available online 16 December 2025

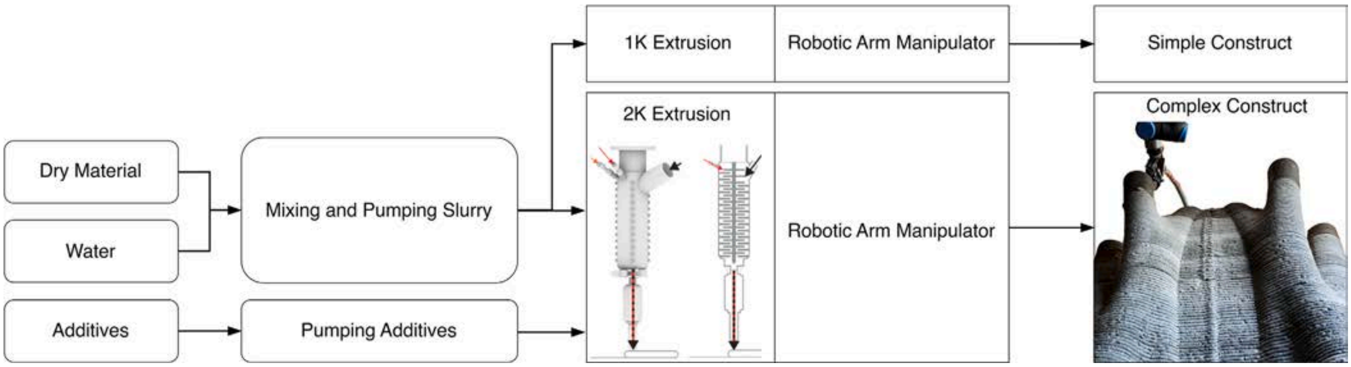

Fig. 1. Comparative schematic of 1K and 2K extrusion systems in 3DCP, illustrating how inline mixing of admixtures in 2K systems enables fine-tuned control of material properties and the production of complex parts.

24]. Imbalances in these parameters can quickly lead to system failure in the form of clogging and construct failure in the form of elastic buckling or plastic yielding during 3D printing [15,25–27].

Because 3DCP is used primarily to build large-scale structures and building elements, failures become extremely costly and render the widely adopted trial-and-error approach for quality control inadequate [7,28–31]. To prevent premature construct or system failure, while also ensuring construct quality; it is imperative to measure, monitor, and control the evolution of time-dependent material properties of concrete in real-time throughout the 3D printing process.

Achieving advanced control over the behavior of the concrete time-dependent material behavior requires the use of two-component (2K) extrusion systems [32,33]. The existing 3DCP printhead technologies are mainly one-component (1K) and 2K systems (Fig. 1). In both systems, a concrete slurry is pumped to the printhead, depositing the material layer-by-layer. The key difference in the 2K system, relative to a 1K system, is its rapid stiffening of a concrete mix at the 2K mixing head using chemical accelerators. An accelerator is pumped separately and mixed with the concrete slurry in the 2K mixing head just before deposition, allowing precise control over the material's open and setting times [2,33–35].

2K systems provide several advantages over 1K systems, particularly in enabling the manufacturing of complex geometries that require faster concrete setting [36–40]. However, the addition of a separate mixing step in which concrete additives are introduced in 2K systems introduces complexities that do not exist in 1K systems. This extra step has significant implications for material homogeneity and overall health of the fabrication system, as it introduces multiple new failure points in the setup, such as the concrete hose inlet to the 2K mixing chamber, the additive inlets to the 2K mixing chamber, and the inline mixing chamber itself.

Our research focuses on data collection and modeling to prevent failures in the 2K systems. This paper addresses the first milestone: effectively detecting anomalies and monitoring the health of 2K 3DCP systems. To achieve this, novel heterogeneous sensing and condition monitoring strategies must be developed and tailored to the unique requirements of 2K 3DCP [10,30,41,42].

1.2. From trial-and-error to first-time-right

1.2.1. Problem statement and related work

Current 3DCP processes still rely heavily on human intuition and manual parameter tuning to maintain print quality and prevent failures. Human operators visually inspect the extruded material and adjust key parameters, such as the water and accelerator dosage, the pump rate, or the nozzle speed, based on heuristic judgments. This manual approach relies heavily on the operator's expertise, which can delay responses to system or manufacturing errors that require real-time intervention. Human observers detect problems at varying resolutions and temporal rates, leading to process delays and the potential for increased system failures, construct dimensional inaccuracies, or construct failures. Complex geometries require a more sophisticated level of monitoring that can predict and thus preempt errors before they manifest. Complex geometries are also more vulnerable to disturbances or even fluctuations in the operating state of the extrusion system (e.g. variations in flow stability, pressure response). By the time an operator notices an anomaly and acts to correct it, irrecoverable errors may already have occurred. Therefore, reliance on manual parameter tuning and human monitoring constraints 3DCP to simple geometries, such as rectangular walls; thus restricting the fabrication of materially optimized elements that inherently entail complex geometries [2,9].

Multiple studies have been conducted to address the limitations of current manual condition monitoring approaches in 3DCP. However, the existing literature focuses mainly on two main questions, the first being material evaluation, quantified through metrics that describe desirable material properties. Mixing motor power has been used to monitor slurry homogeneity, as changes in power consumption can indicate variations in slurry consistency, while pumping motor power provides insights into the pumpability of the slurry by indicating flow resistance within the system [43,44]. Slurry hydration after extrusion can be assessed through temperature and moisture measurements [45]. Infrared thermography uses thermal imaging to evaluate material maturity based on temperature, allowing for the estimation of reactivity and strength development [46], whereas near-infrared spectroscopy provides an in-line method for estimating material surface moisture in extruded material, which is critical for ensuring adequate inter-layer bonding [45].

Another focus is construct evaluation, assessed by monitoring geometric fidelity and dimensional accuracy during the deposition stage [47–52]. Vision-based sensing modalities, including 2D and 3D vision, offer the highest spatial and temporal resolution for real-time construct monitoring [10,53]. These modalities can rapidly capture large volumes of data to generate accurate and comprehensive spatial information [54–57] and efficiently detect anomalies using computer vision techniques [58–60]. 2D vision typically employs cameras mounted on the printhead for sequential layer imaging [61,62] or fixed above the build platform to capture entire layers in a single frame [63,64]. Cameras oriented perpendicularly to the platform normal have also been used for sidewall inspection to detect deformations, layer misalignments, and flow deficiencies [65]. Furthermore, 3D vision provides additional depth information through structured light or stereoscopic systems fixed relative to the platform [66–69], or through laser triangulation sensors mounted on the printhead, which scan the surface/part to generate point clouds that capture the complete profile of the printed layer or construct [70,71].

As a result, the collected data remain compartmentalized within these two focus areas. However, material and construct performance are closely coupled with the underpinning extrusion process, and errors within the system can significantly influence subsequent material properties and construct outcomes. However, there remains a significant gap in research on real-time monitoring of 3DCP system health, particularly in detecting whether the system is operating in an anomalous condition or within normal operating parameters, which is crucial to achieving comprehensive quality assurance in 3DCP alongside material and construct assessments.

Furthermore, very limited research has been conducted on 3DCP sensor instrumentation in the system [72,73], particularly in identifying which data types best detect system anomalies, which sensors can be effectively combined, and how different datasets can be integrated. Several industrial systems have integrated sensors for process monitoring: for example, COBOD [74] uses cameras for live inspection, Vertico's Accelerator Printhead [75] incorporates sensors for real-time monitoring of pressure, temperature and humidity, and ICON [76] reports the use of sensors to track environmental factors and their effects on material processing. However, details on sensor types, integration strategies, and data utilization methods remain limited, as most industrial implementations are not systematically disclosed in the scientific literature and their full technical specifications are not publicly available. In the absence of systematic methods to identify the most suitable sensors for monitoring various aspects of the 3DCP process - and to manage how these sensors collectively capture data - the resulting datasets are often complex and fragmented. The datasets typically include varying dimensions, modalities, and structures, which further complicates the joint analysis and hinders the extraction of valuable insights. These gaps hinder the ability to detect anomalies, predict failures, and adjust parameters for quality control, perpetuating reliance on trial-and-error methods and impeding the advancement of automated and intelligent 3DCP systems.

1.2.2. Paper goal and contributions

This paper extends the existing literature by introducing a comprehensive and generalizable framework for system-level anomaly detection in 3DCP. The framework focuses on the material processing stage, integrating heterogeneous sensing, data collection, and characterization to enable descriptive and diagnostic analyses of the extrusion system rather than post-extrusion construct evaluation. While the methods and framework for anomaly detection are broadly applicable, the metric values used for validation are specific to the feedstocks employed in this study and are therefore not directly generalizable.

The paper pursues this goal through three primary objectives:

- **Systematic Sensor Instrumentation.** The first objective focuses on establishing a clear methodology for identifying non-destructive sensors best suited to gather in-line and online data during the material processing stage of 3DCP. This objective also addresses the practical aspects of sensor integration, including calibration, validation, communication, and synchronization, ensuring that various sensors operate seamlessly within the same 3D printing environment.
- **Data Processing and Analytics.** The second objective focuses on developing robust signal pre-processing methods and data fusion techniques to analyze individual sensor data and combine multiple heterogeneous data streams. The proposed approach seeks to uncover a holistic understanding of the entire 3DCP process. This includes defining steady-state operating conditions from a process perspective and enabling real-time anomaly detection or failure prediction, allowing for swift corrective actions.
- **Experimental Validation of the Framework.** The third objective involves conducting case studies to demonstrate the practical viability of the framework in real-world 2K 3DCP implementations. This includes physically integrating the selected sensors, collecting and processing data in ongoing printing scenarios, and evaluating the system's effectiveness to quickly detect anomalies and anticipate potential failures. Using pre-selected successful case studies, this paper provides empirical evidence of the contribution of the framework to improving the overall reliability and efficiency of the process.

Achieving these objectives ultimately results in the following primary contributions of the paper:

- A generalizable framework for real-time anomaly detection and diagnosis in 2K 3DCP systems. Generalizability refers to the methodological pipeline and model classes; process deployment specific thresholds, control limits, and other machine and material dependent parameters must be empirically calibrated for each new scenario.
- A structured approach to identify, calibrate, and integrate heterogeneous sensors, ensuring synchronized data collection and analysis.
- A foundation for future research toward predictive monitoring and automated error prevention in 3D printing of complex geometries and large-scale structures.

2. Methods

The methodology of this work is based on an experimental approach to collect real-time data from physical experiments. This approach is essential because existing models for simulating 3DCP are computationally expensive and models that describe the process with the required accuracy are not yet available [77–81]. To circumvent the Sim-to-Real gap [82–85], it is crucial to perform and evaluate these experiments under real conditions. The details and findings of these experiments are presented in Section 3.

Section 2 details the underlying methods for conducting the experiments. This section is divided into four subsections: system setup for extrusion-based robotic 3DCP (Section 2.1), sensor instrumentation (Section 2.2), data acquisition (Section 2.3), and data analysis methods (Section 2.4). The methods presented in this section lay the foundation for the anomaly detection framework.

2.1. System setup for extrusion based robotic 3D concrete printing

The 3DCP setup presented in this paper (Fig. 2) builds on insights from our previous research [2,3,14] and consists of four main subsystems: (a) the MAI MULTIMIX-3D Mixing Pump - a primary slurry mixer and pump, (b) the Accelerator Pump - a liquid additives pump, (c) a 2K Mixing Head used for extrusion, and (d) the KUKA KR120 Robotic Arm - a six-degree-of-freedom robotic arm. Critically, each subsystem features a series of I/O interfaces and modules to facilitate inter-system communication, data collection, and future enhancements through sensor integration.

The MAI MULTIMIX-3D mixing pump can mix up to 50 liters per minute and pump within a range of 1 to 7.5 liters per minute [86]. This subsystem offers a streamlined integrated solution; by combining mixing and pumping in a single unit, the mixing pump eliminates the need to transfer material from a separate mixer to a pump, thus reducing a key source of uncertainty and potential errors stemming from delays or inconsistencies in material delivery.

Although the MAI MULTIMIX-3D mixing pump efficiently delivers the primary slurry to the 2K mixing head, incorporating liquid additives requires a separate dedicated pumping system. Peristaltic pumps are commonly used for such applications [87–89]; however, their continuous compression and relaxation can introduce pulsations into the liquid stream, potentially causing slurry to backflow from the 2K mixing head into the liquid accelerator pump line. This limitation makes peristaltic pumps unsuitable for this use case, necessitating the

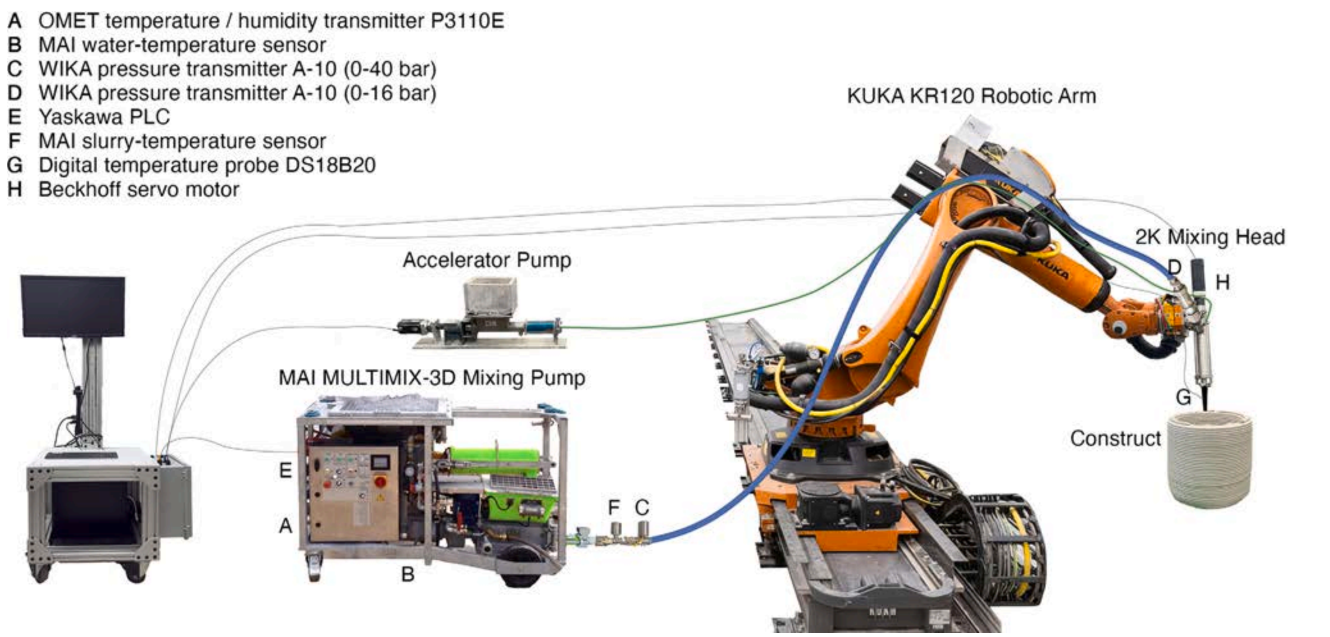

Fig. 2. Schematic overview of the 3DCP setup and sensor integration layout used in this research for data collection. The system combines a KUKA KR120 robotic arm with a 2K mixing head, MAI MULTIMIX-3D mixing pump, and accelerator pump. Various sensors (A–H) are integrated throughout the system to enable inline monitoring of temperature, humidity, pressure, and power conditions during the 3DCP process.

adoption of a continuous-flow pump. To overcome these challenges, we designed and built a custom pump that was adapted to the requirements of the system. An AM8132 Beckhoff servo motor [90], coupled to a Neugart PLE gearbox with a 32:1 gear ratio [91], drives the rotor of a progressive cavity pumping element. This design delivers pulsation-free flow ranging from 0 to 10 liters per minute. In addition, precise control of the servomotor ensures highly accurate additive dosing, thus optimizing the overall performance of the system.

Primary slurry and liquid additives are mixed inline using a custom-built 2K mixing head or end effector. The end effector features two primary inlets: one for the primary slurry and one for the liquid additive. These inlets lead to a mixing chamber with a volume of 0.5 l. At a pumping rate of 1 liter per minute for the primary slurry, this chamber provides a residence time of 30 s, ensuring adequate mixing. The mixing chamber consists of two key components: a series of pins acting as a stator and a mixing rotor. The rotor is powered by an AM8033 Beckhoff servo motor [92], which is coupled to a Neugart PLE gearbox with a 20:1 gear ratio [91]. To host the 2K end effector, the KUKA KR 120 R2700 industrial robotic arm [93] was selected. With a payload capacity of 120 kg and a reach of 2700 mm, this robotic arm is capable of supporting the weight of the end effector, including the additional load from the concrete hose and the concrete within the mixing chamber. Furthermore, the extended reach of the KUKA robotic arm enables the fabrication of large-scale constructs, making it well-suited for the experiments described in this paper.

2.2. Sensor instrumentation

Sensor instrumentation in 3DCP requires careful selection of sensors based on their suitability to monitor specific aspects of the process, shown in Table 1, as well as their ability to provide precise and repeatable measurements. The instrumentation method begins by defining clear requirements, followed by selecting sensors that match the intended use cases and in the desired measurement range. Once selected, the sensors are installed at the optimal locations to monitor the parameters that are representative of the process. Once installed, the sensors undergo an initial calibration and baseline testing under a range of operating conditions to verify their accuracy, ensuring traceability to recognized standards (e.g., ISO 17025 [94]).

2.2.1. Sensor requirements and selection

The selection of appropriate sensors for 2K 3DCP requires accurate real-time monitoring of key process parameters, including environmental conditions, slurry pumpability, hydration reactions, and slurry workability.

Environmental conditions, including air temperature and humidity, can have an impact on the rheology of the slurry and the setting behavior during the 3DCP process [99–102]. Fluctuations in environmental conditions can alter the way the slurry hydrates and solidifies, potentially affecting both the workability and the performance of the final construct. To ensure stable and representative measurements, the OMET transmitter P3110E [95] has been pre-installed in the mixing pump. The temperature of the mixing water is also critical, as variations can change the initial temperature of the fresh slurry and therefore affect its setting kinetics [103–105]. To achieve this, an MAI water temperature sensor [86] has been installed at the water input of the mixer to continuously measure the temperature of the fresh water entering the mixer.

During pumping, the fresh slurry behaves as a Bingham plastic fluid, exhibiting both yield stress and plastic viscosity [106]. If the yield stress and viscosity exceed a certain threshold, the material cannot be properly pumped [107,108]. Monitoring real-time pressure helps determine whether the material remains pumpable or if clogging is happening. In addition, early detection of pressure fluctuations prevents defective prints due to changes in material properties [107]. Consequently, a pressure sensor must measure the pressure directly at the point where the slurry is transitioned from the container to the printhead through the hose. This sensor must also be properly sealed to ensure water-tightness and to withstand direct contact with fresh concrete. The selection of the pressure sensor range at the mixing head inlet was guided by the rheological parameters of the slurry, which govern the pressure drop along the hose, leading to a higher pressure at the inlet and a lower pressure toward the outlet. Pre-printing rheological material tests indicated that the outlet pressure for safe operation should remain below 15 bar, and exceeding this threshold would signal a significant issue. Consequently, a higher resolution WIKA pressure transmitter A-10 (0–16 bar) [96] was chosen for the lower pressure end, while a WIKA pressure transmitter A-10 (0–40 bar) [96] was chosen to protect against overpressure and to match the pump's maximum

Table 1
Table of monitored processes, signals, and sensors.

Monitored process	Signal	Sensor location	Sensor model
Environmental conditions	Humidity Air temperature	Mixing pump	OMET transmitter P3110E [95]
	Water temperature	Mixer inlet	MAI water-temperature sensor [86]
Pumpability	Pressure	Pump outlet 2K mixing head inlet	WIKA pressure transmitter A-10 (0–40 bar) [96] WIKA pressure transmitter A-10 (0–16 bar) [96]
	Power	Mixing pump	Yaskawa PLC [97]
Hydration reaction	Slurry temperature	Pump outlet 2K mixing head outlet	MAI slurry-temperature sensor [86] Digital temperature probe DS18B20 [98]
Workability	Torque	2K mixing motor	Beckhoff servo motor AM8033 [92]

operating limit of 40 bar. Furthermore, both pressure sensors are inserted into rugged steel with an internal membrane, enabling them to withstand exposure to high-solid materials.

The electrical power consumption of the pump drive motor provides an indirect but valuable insight into the characteristics of the slurry flow, as power consumption reflects the energy required to pump the material [109]. Under constant flow, changes in power consumption can reveal alterations in viscosity or flow resistance. In particular, a gradual increase in the required power may occur if hydration reactions substantially increase the yield stress and viscosity. In addition, excessive power use can suggest blockages or elevated friction, while an unexpected drop could indicate equipment malfunctions or insufficient material loading. Monitoring the electrical power consumption of the pump drive motor can be performed using a Yaskawa Programmable Logic Controller (PLC) [97].

The temperature of fresh slurry offers information on the concurrent evolution of its rheological properties during early-age hydration [34, 110], as the yield stress and viscosity can change rapidly with the progression of exothermic reactions [46]. The resulting temperature profile provides a direct indicator of both the rate and extent of hydration [111]. To capture rapid exothermic reactions that occur during early-age hydration, temperature sensors must provide a quick response and have a wide and stable measurement range capable of detecting temperatures from ambient levels up to at least 50–60 °C. These sensors must be able to withstand chemical reactions, requiring corrosion-resistant materials and robust construction. They should also feature water-tight sealing (e.g. IP67 or higher) to protect against high moisture levels and fine solids that may cause measurement drift. Two temperature sensors are installed at key points in the system. The first sensor, an MAI slurry-temperature sensor [86], is designed with the same inner diameter as the delivery hose, allowing it to measure the initial slurry temperature without disrupting flow. Meanwhile, the second sensor, a compact and waterproof digital temperature probe DS18B20 [98], is inserted directly into the 2K mixing head, allowing for localized temperature monitoring.

The torque of the inline mixer is a useful measurement to assess secondary mixing behavior [43,44]. A stable torque level typically indicates a uniform distribution of aggregates, binders, and additives, leading to consistent performance in downstream processes. In contrast, significant deviations or fluctuations in torque can signal variations in material composition or incomplete mixing. The torque of the Beckhoff AM8033 inline mixer servo motor [92] is recorded to provide insight into the inline mixing process.

2.2.2. Sensor installation and physical deployment

Strategic placement and secure installation of each sensor to ensure accurate and representative data collection is important, as shown in Fig. 2.

OMET air temperature and humidity transmitters are placed away from direct sources of heat and moisture to avoid skewed readings [112]. The proximity of the sensors to the mixing station ensures that the captured environmental data reflect the actual process conditions. In addition, the MAI water-temperature sensor is submerged into the water pipe to track variations in the temperature of the mixing water.

Pressure sensors must be installed to capture pressure signals through the hose. One WIKA pressure transmitter A-10 (0–40 bar) is placed at the pump outlet to record initial pumping conditions, while another WIKA pressure transmitter A-10 (0–16 bar) records pressure just before the slurry enters the 2K mixing head.

A PLC-based monitoring setup is employed in both the pumping system and the 2K mixing head to track motor performance. By recording the use of electrical power from the pump drive motor in real-time, the PLC provides an indirect indicator of the flow behavior of the material. Meanwhile, torque data from the Beckhoff servomotor offer continuous feedback on mixing performance, revealing slurry problems in the 2K mixing head.

Temperature sensors are installed at two critical points: the MAI slurry-temperature sensor is integrated at the outlet of the slurry container, measuring the material temperature immediately before pumping. The digital temperature probe DS18B20 is placed in the 2K mixing head directly before extrusion to monitor temperature variations resulting from hydration reactions and the addition of accelerators or retarders. Ensuring direct contact with the material at both locations enables accurate detection of temperature changes that can affect material performance.

2.2.3. Sensor calibration and testing

To maintain measurement accuracy and reliability, all sensors undergo factory calibration. Factory precalibrated sensors, including the OMET transmitter, WIKA pressure transmitters, MAI water and slurry temperature sensors, and the mixing pump power measurement unit, arrive with predefined settings optimized for their intended application. The digital temperature probe DS18B20 and the PLC-based torque monitoring system are also calibrated exclusively at the factory to ensure accurate performance under anticipated operating conditions.

To verify the accuracy and reliability of the sensor data, baseline testing is performed before full deployment. Initial readings are compared against reference instruments to confirm sensor precision, and trial runs are performed under varying conditions, including different flow rates and temperature settings, to evaluate the performance of the monitoring system. These tests ensure that all sensors are correctly installed, properly calibrated, and capable of delivering accurate data for real-time anomaly detection.

2.3. Data acquisition

To enable real-time monitoring, it is essential to establish a pipeline for data acquisition. In the context of 2K 3DCP, it is necessary to test and evaluate a wide variety of sensors, many of which have differing sampling rates and data structures [10,61,70,113]. A network has been developed in which both sensing and process control devices communicate with a central database. This database aggregates the information and stores it in a manner that, despite the heterogeneous nature of the data, enables homogeneous analysis. In the current system, approximately 70 data signals are initially collected, which are then filtered down to 9 signals that provide a comprehensive view of the system's state.

The central database is a high-performance laptop that communicates directly over a TCP/IP network [114,115] with all other devices. Connections with other devices include OPC-UA [116] over TCP, SSH data transfer tunnels [117], UDP streaming [118], and custom software that interfaces with remote nodes.

Each data stream is collected individually. The OPC-UA devices are queried at set intervals, while video devices with computer interfaces stream data via UDP back to the central database. For devices lacking a dedicated commercial off-the-shelf network solution, a Raspberry Pi (RPi) aggregator is used [119], with the server retrieving the data through SSH. Custom software is developed to handle data collection and aggregation on the server, storing the data as time-stamped JSON files [120].

The main challenges with this solution include time synchronization, diverse sampling rates, and the overhead of preprocessing requirements. Time-synchronization issues arise from the reliance on the data source, rather than the central database, to report accurate timestamps. Instead of generating timestamps on data receipt, the central database relies on the sensor or sensor aggregator (e.g., the RPi) to report the timestamp, minimizing the impact of network delays on predictions. However, improper calibration of the sensor clocks occasionally necessitated manual synchronization post-experiment. For the experiments presented here, three of the sensors operated on the same device and were inherently synchronized, while the Motor Torque (2K Head) signal required manual alignment. This was accomplished by calculating the offset of the recording device before each experiment and verifying alignment against manually recorded initiation times. Signals that could not be reliably synchronized were excluded, and thus only a subset of the collected data is reported in this study. Moving forward, the system will incorporate a network time protocol (NTP) server to align all devices on the same network. Because each reporting device can then self-align to the NTP clock and self-report timing, this approach will eliminate manual alignment and enable robust, automated synchronization across heterogeneous sensors.

Various sampling rates create difficulties when performing discretized point analysis on multiple data streams, requiring the data to be resampled. Sometimes data are captured at uneven sampling intervals, so interpolation [121–123] can be used to standardize sampling and create a homogeneous dataset from the different sensors.

Finally, some data require preprocessing before use. In some cases, this is done at the aggregator, such as converting voltage readings to temperature measurements. For other data sources, such as PLC registers, lookup tables are referenced. Although each preprocessing step is minor on its own, collectively, the preprocessing steps introduce significant overhead at scale. To accommodate hardware limitations, these processes are optimized to ensure that the central database can efficiently handle all data streams.

2.4. Analysis methods

This section provides a brief overview of the analysis methods that are applied to the different data streams for feature identification and anomaly detection.

2.4.1. Signal processing

Signal processing is a broad field with numerous techniques and procedures [124]. The process documented in this section focuses on applying signal processing techniques to identify features that can be directly attributed to changes within the 2K 3DCP system, referred to as critical features. Furthermore, if a critical feature can serve as an early alert for anomalous system behavior, it is designated as a key indicator. In this paper, we present four techniques that have proven effective in identifying key indicators for anomaly detection in 2K 3DCP. Fig. 3 illustrates the workflow of the process. Assuming all collected data are time series and can be uniformly synchronized along the time axis, this process can be applied.

The workflow begins with data collection, which includes time series signal data from the 2K 3DCP system and a timeline of events that are manually recorded during system operation with accurate timestamps. Data are synchronized through interpolation along the time axis in uniform intervals, allowing a standard approach to data processing [122,123,125,126]. Signal analysis is performed as a set of techniques individually applied to each signal to expose signal features. In parallel, a key event timeline is constructed by discretizing the manually recorded events along the time axis. These events are then directly compared to the output of each signal analysis technique to correlate whether an exposed signal feature qualifies as a critical feature. A critical feature should consistently identify an event, or class of events, on the key event timeline. If an anomalous event can be positively identified through a critical feature, this critical feature becomes a key indicator for anomaly detection within the system.

The analysis techniques used in this work are not an exhaustive list; however, these techniques have proven effective in exposing critical features and key indicators for the system described in Section 2.1. The four techniques applied in this research include: frequency analysis, amplitude envelope detection, linear versus exponential curve fitting, and magnitude deviation analysis.

Frequency analysis is applied using the Short-Time Fourier Transform(STFT) [127] and overlapping windows of time [127–129]. This is represented by the following equation:

$$X(t,f) = \int_{-\infty}^{\infty} x(\tau) w(\tau - t) e^{-j2\pi f \tau} d\tau \tag{1}$$

where $x(\tau)$ is the original signal, $w(\tau - t)$ is the windowing function, and $e^{-j2\pi f \tau}$ represents the Fourier transform. Careful window selection is required to minimize signal degradation at endpoints [128,129], while ensuring that the window is short enough to capture precise event times. Furthermore, to ensure that this function is robust to changes in amplitude, also called DC bias [128], a high-pass Butterworth filter is applied. The standard form of the high-pass Butterworth filter transfer function in the Laplace domain is:

$$H(s) = \frac{s^N}{\prod_{k=1}^{N}(s - s_k)}$$

where: s_k are the poles of the Butterworth polynomial. $s_k = \omega_c e^{j\frac{(2k+N-1)\pi}{2N}}$ for $k = 1, 2, \ldots, N$, N is the filter order, and ω_c is the cutoff frequency. The cutoff frequency and filter order should be chosen based on the sampling frequency of the data.

Amplitude envelope detection is commonly used to detect amplitude variations associated with underlying phenomena, such as induced pulses in machinery [130–132]. Typically, amplitude envelope detection is performed in the frequency domain using spectral kurtosis [133, 134], which identifies transients through the combination of the Short-Time Fourier Transform (STFT), Wavelet Transform [135], and a set of digital filter banks [136]. For the application described in this paper, the amplitude envelope detection technique requires a sampling rate based on the Nyquist frequency [137], which might not be guaranteed during the synchronization process. A statistical version of this process was created using z-score thresholding [138]. Given a signal with mean μ and standard deviation σ, upper and lower bounds of the envelope are defined:

$$E_{upper} = \mu + k\sigma, \quad E_{lower} = \mu - k\sigma$$

where k determines the confidence interval. This version is not robust to extreme values, as outliers can dominate the variance and cause the envelope to expand unpredictably. By replacing the mean with the median and the standard deviation with the median absolute deviation (MAD) [139], a more robust adaptive envelope is created. This takes the form of:

$$E_{upper} = \mathrm{median}(X) + k \cdot \mathrm{MAD}, \tag{2a}$$

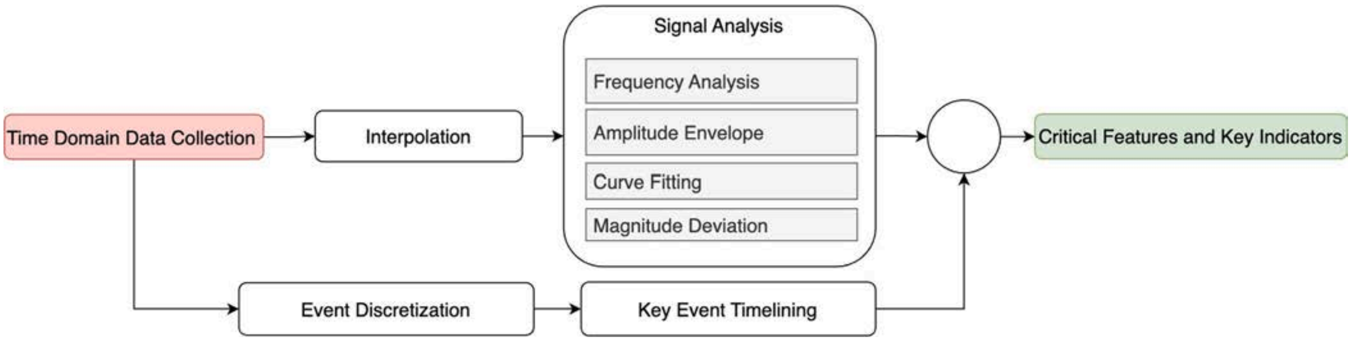

Fig. 3. Critical feature identification workflow for time-series datasets: The dataset is resampled to ensure uniformity and synchronization along the time axis through interpolation. Each signal is analyzed using the four techniques to identify signal features. Events, which are manually recorded during data collection, are discretized along the time axis to create a timeline of key events. This timeline is then compared to the signal features to identify critical features and key indicators.

$$E_{lower} = \text{median}(X) - k \cdot \text{MAD}, \tag{2b}$$

$$\text{MAD} = \text{median}\left(\left|X - \text{median}(X)\right|\right). \tag{2c}$$

Curve fitting, the third technique, is used to identify when a signal can be determined to "fit" a mathematical model [140–143]. Many anomaly detection applications operate under the assumption that, under normal conditions, a signal will closely match a known mathematical model [144–147]. For the 2K 3DCP system described in Section 2.1, it was found that the normal rate of change of most observed signals stabilizes to a linear trend. Using this assumption, the system is considered to be in an anomalous state when confidence in this linear behavior falls below a threshold.

To evaluate linear confidence, a two-stage analysis procedure is used. First, the filtered signal $y(t)$ is segmented into overlapping windows of duration W_s. Within each window w, a linear model is fit using least squares [148–150]:

$$y(t) \approx \alpha_w t + \beta_w, \quad t \in I_w, \tag{3}$$

and the magnitude of the slope is extracted to represent the local rate of change:

$$s_w = |\alpha_w|, \qquad t_w = \frac{1}{|I_w|} \sum_{t \in I_w} t. \tag{4}$$

This produces a new time-series signal $\{(t_w, s_w)\}$ that characterizes the local dynamics of the original measurement.

In the second stage, the slope signal is itself segmented into overlapping windows j. A linear model is then fit to each segment to evaluate whether the slope evolves consistently:

$$\hat{s}(t) = a_j t + b_j, \tag{5a}$$

$$R^2_{\text{lin},j} = 1 - \frac{\sum_{w \in J_j} (s_w - \hat{s}(t_w))^2}{\sum_{w \in J_j} (s_w - \bar{s}_j)^2}, \tag{5b}$$

where J_j indexes the slope samples within window j, and $\bar{s}_j$ is their sample mean.

An anomaly is detected when the confidence in the linear trend falls below a defined threshold:

$$R^2_{\text{lin},j} < \tau_{R^2}. \tag{6}$$

The final technique described in this section is magnitude deviation analysis. Using the model from Eqs. (3)–(6), this technique identifies a large and rapid change in magnitude that may still be linear. The detection process described for curve fitting fails to identify an anomaly in the case where the growth is linear but too large for stable operation. The detection approach shown in Eq. (7) accounts for this case.

$$\hat{y}_{\text{lin}}(t) = at + b, \quad \text{with rapid growth detected if} \quad |a| > \tau_s. \tag{7}$$

where τ_s represents a user-defined threshold.

2.4.2. Guidelines for targeted signal processing

Each of the techniques described above can be applied to any time-series signal that meets the synchronization criteria. Table 2 provides some key examples studied in Section 3. These specific detection thresholds are not generalizable outside of the test system described in this work. Instead, this framework aims to show how to discover this criterion. The tuning of the fault detection metrics will be based on the system and material used. For example, the power band used for temperature frequency analysis is derived from the sampling time of the system and the anomaly observed in a visual review of graphed signals. The amplitude envelope used a 95% confidence interval, which might be too loose or too tight for other applications. Based on empirical observations, classifying signals by a few key attributes can help identify which technique(s) are most likely to yield a critical feature. These attributes can generally be categorized into three types: Gradual Changes, Step Transitions, and Rapid Fluctuations.

Gradual Changes: In continuous systems, such as the pump system used in this work, once the system reaches steady state, future measurements within the same task state should have little to no variation [151]. Deviations from this expected behavior are considered anomalous [152–154]. Frequency analysis and magnitude deviation analysis are effective tools for detecting this type of anomalous behavior. For example, for the 2K 3DCP system discussed in Section 2.1, temperature, pressure, and ambient humidity all exhibit gradual changes and are best analyzed using frequency analysis or magnitude deviations.

Step Transitions: Some signals exhibit abrupt jumps to new step values, which may or may not oscillate around these values. These transitions are typically sharp and occur suddenly during the process. Detecting anomalous transitions in step signals can be achieved through amplitude envelope detection. Although not explored in this paper, curve fitting to a step model, as opposed to a linear model, could also provide valuable insight for this type of signal. Examples of this behavior can be seen in the torque of the mortar pump, the electrical current of the pump, and the water rate signals within the concrete mixer.

Rapid Fluctuations: Signals with rapid fluctuations often represent either noisy sensors or oscillating signals. Amplitude envelope detection can help capture the general trend of the signal, while frequency analysis can be used to identify anomalies, especially if the fluctuations are predictable or harmonic in nature. Examples of signals that exhibit this type of behavior from the 2K 3DCP system include the electrical power of the concrete mixer and the torque of the 2K mixing head.

Table 2
Notable detection criteria.

Method	Key signals used	Fault detection metric/Threshold	Example test (s)	Formula Ref.
Frequency analysis (STFT)	Slurry temperature (pump)	Avg. power in 0.05–0.25 Hz band > −25 dB	Test 2 (Fig. 5)	Eq. (1)
Amplitude envelope detection	Torque (2K mixing head)	Median $\pm k \cdot$ MAD, $k = 2.97$ (95% CI)	Test 7 (Fig. 6)	Eqs. (2a)–(2c)
Curve fitting (Linear Fit)	Slurry pressure (pump)	$R^2_{\text{lin}} < 0.5$ with slope $\lvert\alpha\rvert < 0.02$	Test 5 (Fig. 7)	Eqs. (3)–(6)
Magnitude deviation	Slurry pressure (pump)	Slope $\lvert\alpha\rvert > 0.02$ beyond tolerance band	Test 5 (Fig. 8)	Eq. (7)

Table 3
Experiments setup.

Test ID	Dry material	Additive	Construct
1, 2, 3	Sikacrete-752 3D mix	Sigma-Aldrich LUDOX HS-40 colloidal silica	Cylinder (diameter: 400 mm and height: 500 mm)
4, 5	Quickcrete ASTM Type I Ordinary Portland Cement, Boral Micron3 fly ash, fine silica	Sigma-Aldrich LUDOX HS-40 colloidal silica	Zigzag extrusion (length: 300 mm, width: 300 mm and height: 30 mm)
6, 7, 8, 9	Sikacrete-752 3D mix	Sigma-Aldrich LUDOX HS-40 colloidal silica	Box (length: 250 mm, width: 250 mm and height: 500 mm)

Table 4
Observed status of monitored signals for each test.

Test ID	Motor Power (Pump)	Slurry Pressure (Pump)	Slurry Temperature (Pump)	Motor Torque (2K Head)
1	Healthy	Healthy	Healthy	Healthy
2	Anomalous	Anomalous	Anomalous	N/A
3	Healthy	Anomalous	Anomalous	N/A
4	Healthy	Healthy	Healthy	N/A
5	Anomalous	Anomalous	Anomalous	N/A
6	Healthy	Anomalous	Anomalous	Anomalous
7	Healthy	Anomalous	Healthy	Anomalous
8	Healthy	Healthy	Healthy	Healthy
9	Healthy	Anomalous	Healthy	Anomalous

N/A - The signal was unable to be recorded.

* Used only for model validation

3. Experiments

In this section, the analysis techniques described in the Methods section are applied to experimental data to detect healthy and abnormal behavior. The experimental study consists of nine tests that include 3D printing of three different construct types using two different material formulations, shown in Table 3. Three cylindrical constructs (400 mm in diameter and 500 mm in height) and four box-shaped constructs (250 mm in length, 250 mm in width, and 500 mm in height) are produced using Sikacrete-752 3D mix [155]-the industry-standard commercial mix widely adopted in practice-combined with the additive Sigma-Aldrich LUDOX HS-40 colloidal silica [156] at the 2K mixing head. Two zigzag-shaped structures (300 mm in length, 300 mm in width, and 30 mm in height) are fabricated using a custom house-made dry mix comprising ASTM Type I OPC from Quickcrete [157], Boral Micron3 fly ash [158], and fine silica sand of sizes 0.2–0.6 mm [159] combined with the additive Sigma-Aldrich LUDOX HS-40 colloidal silica in the 2K mixing head. The water-to-cement ratio, water-to-binder ratio, sand-to-binder ratio, and additive-to-binder ratio for this custom dry mix are set at 0.65, 0.33, 0.35, and 0.01 respectively. Across the nine prints, the pump flow rate is 2.4 L/min , layer height is 10 mm, and robot travel speeds range from 150 mm/s to 300 mm/s. It should be noted that the specific construct geometries are not the focus of this study, as the objective is to evaluate the ability of the proposed monitoring framework to detect healthy and abnormal behavior during the process of 2K 3DCP. The developed approach can subsequently be applied to the 3D printing of geometrically complex elements.

During these tests, human operators record their observations of the state of the system. The states are identified through manual review of anomalous signal patterns that appear in tests with observed system failures and yet are absent in tests that did not experience failure. These observations, shown in Table 4, became the labels that are used in the development and validation of anomaly detection. The Fig. 4 illustrates that tests primarily containing healthy signals show no visible anomalies on the printed constructs, whereas anomalous patterns can be associated with deviations related to material properties or extrudate dimensions, which subsequently affect the final construct. It should be noted, however, that not all process anomalies manifest as visible defects in the printed parts, and a comprehensive understanding of how different types of process anomalies influence the construct requires further investigation.

3.1. Results and discussion: Identifying critical features from experimental data

3.1.1. Signal features during normal operation state

Understanding normal operation is critical to setting the benchmark for stable system behavior, state transitions of the system, and anomalous system conditions. To characterize the operations, the observed signals were labeled health or unhealthy. Regions within a healthy signal that may exhibit anomalous behavior, such as startup or state change transitions, were defined and separated from the data streams prior to running the anomaly detection analysis. Fig. 5 shows examples of healthy process data from Test 1, which did not experience significant errors or anomalies. The first half of the graph shows the

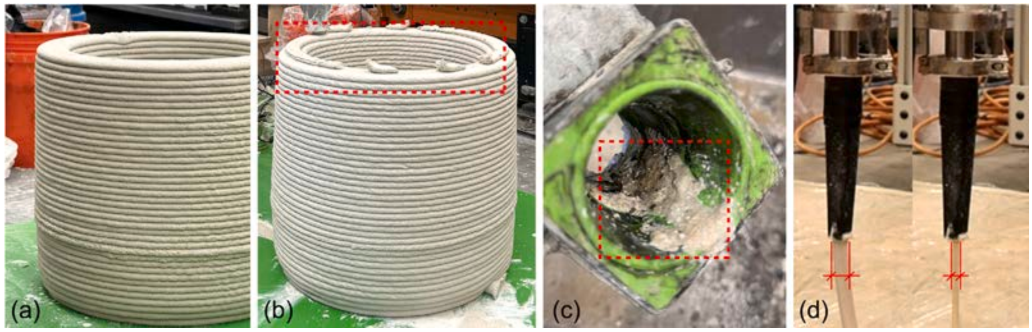

Fig. 4. (a) Test 1, which primarily contains healthy signals, shows no visible anomalies on the printed constructs. (b) Test 3 exhibits pump clogging that causes discontinuities in the extrudate; corresponding anomalies are observed in slurry pressure and temperature data. (c) In Test 5, material segregation was observed, accompanied by anomalies across motor power, slurry pressure, and slurry temperature signals. (d) Test 6 shows significant nozzle head clogging, where the extrudate cross-section becomes noticeably smaller than under normal operation, indicated by anomalies in motor torque.

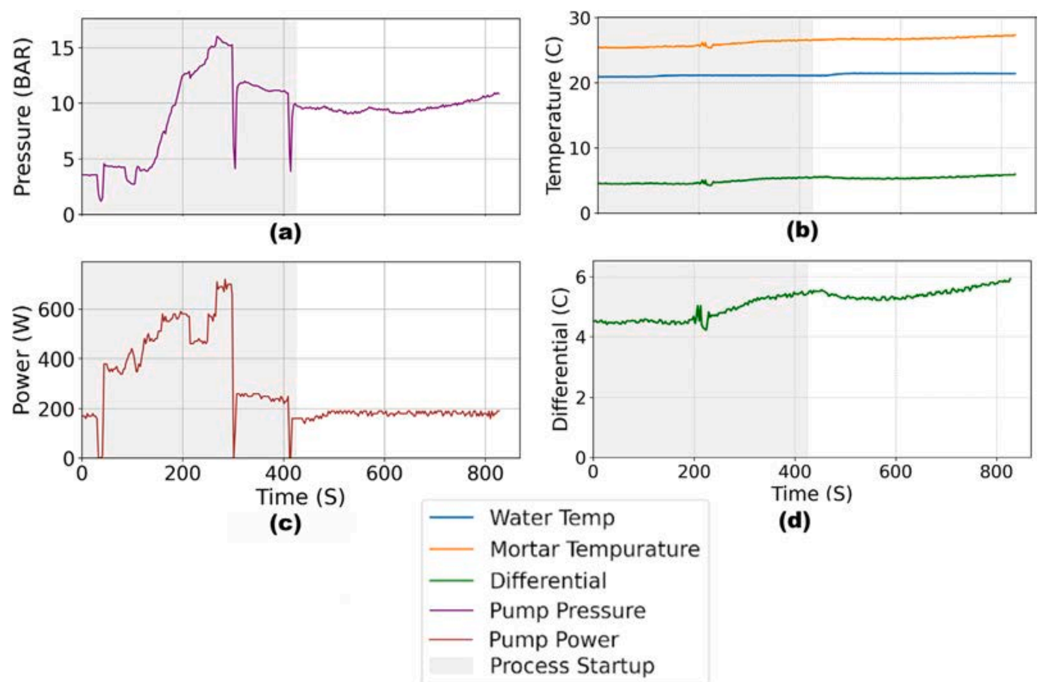

Fig. 5. Healthy system data: (a) Healthy slurry pressure (pump) with less than +/−1 bar variance. The gray shaded region represents the startup process that is not included in the analysis. (b) Healthy slurry temperature (pump) data. Water temperature is subtracted from the slurry temperature (pump) to remove environmental bias (differential) with +/−3 degrees variance after steady state. (c) Healthy motor power (pump) signal. After startup shown in gray, the motor power (pump) stabilizes around a single value with minor noise. Although not shown, motor power (pump) can dip to zero due to idling processes of the controller, but should quickly jump back to a steady state value. (d) Zoomed in signal from the differential of slurry temperature (pump) and water temperature. Note the minor noise spike in the startup region shaded in gray. This is considered normal in startup but would be an anomaly otherwise.

startup process before steady state starting at 425 s. Following the transition to steady state, all of the signals demonstrate properties of stable printing.

3.1.2. *Low frequency noise for anomaly detection*

As discussed in Section 2.4.2, the temperature of a continuous-flow material should remain stable assuming that there are no significant process or baseline changes. However, in Fig. 6(a), the slurry temperature (pump) signal begins to experience an increase in signal noise at 623 s. This behavior is present only when the system is undergoing a state change or during an abnormal operation. In this specific case, the system has a minor clog in the concrete slurry hopper. It is hypothesized that this anomalous feature is created by inconsistent flow against the temperature sensor probe. The velocity of different regions in a concrete pipeline, as well as the effects of discontinuous pumping characteristics, have been studied in other papers [160,161], but for the purposes of this application, it is sufficient to know that the feature occurs only when the system is not in steady state. Using the technique described in Section 2.4 by Eq. (1), Fig. 6(b) shows the average power of the temperature signals in a frequency range of 0.05 to 0.25 Hz, converted to decibels to facilitate easier comparison between signals with varying amplitudes. The threshold value of −25 dB is created by assessing the slurry temperature (pump) signals of the tests [1,4] and selecting a value high enough to remove these tests from detection while still identifying the anomalies in the slurry temperature (pump) signals from tests [2,3,5,6]. Fig. 6(b) illustrates that the noise in the signal exceeds the −25 dB threshold at 560 s. The clog associated with this increase in noise is visually detected by the operators when it affects the extrusion at 750 s. Video records show a small chunk of hardened mortar is knocked into the wet hopper at 550 s, which is the root cause of the anomaly. For this example, the identified anomalous feature shows the sensitivity of automated detection by identifying the

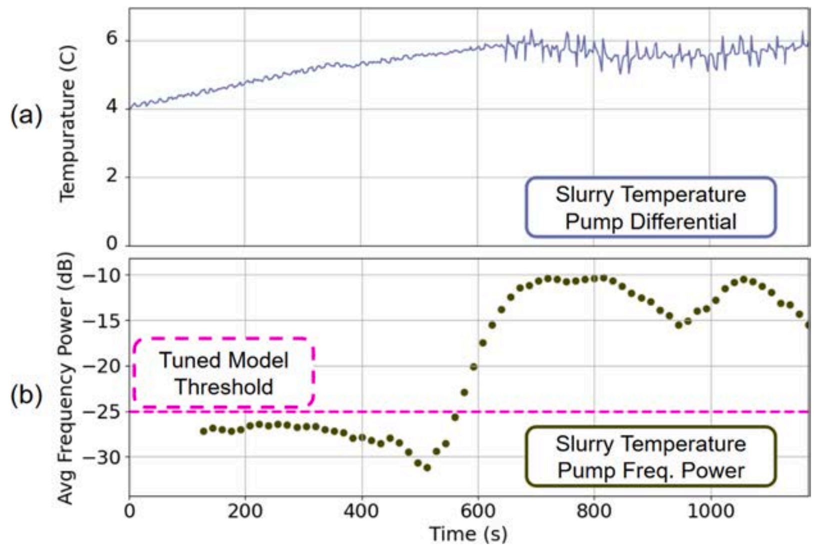

Fig. 6. Frequency response analysis: Plot (a) shows the slurry-water temperature differential from the slurry temperature (pump) signal during test 2, post system start-up. Using Eq. (1) and a frequency range of 0.05 to 0.25, the windowing for frequency analysis plot (b) is set to 128 s with the first average power value starting at 128 s Temperature signals can vary up to 3 degrees, so the ramp from 2 to 6 degrees C in plot (a) between 200 s and 623 s is within normal tolerance. The noise starting at 623 s is anomalous behavior identified by the average power surpassing the −25 dB threshold in plot (b).

anomaly in pump health within 10 s of the signal change, while manual observation lags behind by 190 s.

3.1.3. Envelope breach for anomaly detection

The torque signal of a DC servo motor can have significant noise due to a number of factors such as gear coupling and control loop gains [162], which makes it an ideal signal to be bound with an amplitude envelope. The motor in the 2K mixing head has a torque signal, which can be represented as a step value with harmonic noise. Fig. 7 shows the motor torque (2K mixing head) signal during Test 7. From zero to 180 s, the idle torque is 1.6 Nm with oscillations of +/−0.1 Nm. At 180 s the motor torque (2K mixing head) jumps as the slurry first enters the 2K mixing head and stabilizes again around 1.6 Nm. A statistical envelope from Eqs. (2a)–(2c) is created that will follow small step changes, but allow breaches from large step changes to identify anomalous behavior. The variable $k = 2.97$ is selected from a 95% confidence interval. A rolling median of 128 s is selected to maintain a rigid window on a 2 Hz sampling basis. Any large fluctuations require a full window to stabilize, as shown in yellow shading in Fig. 7. At 420 s, the 2K mixing head sprung a leak, which was detected immediately by a large envelope breach feature. Operators noticed the leak at 453 s, stopping the experiment early. Pure manual observation lags behind the envelope breach detection by 33 s.

3.1.4. Curve fitting for anomaly detection

From the baseline analysis shown in Fig. 5, a healthy pump pressure signal should stabilize around a stable state value with a variance of +/−1 bar. The stable state value can change depending on factors such as pumping speed and environmental conditions, but any such fluctuations should be minor($|\alpha| < 0.02$) with a linear trend. This is characterized using Tests [1,4]. With this baseline, Eqs. (3)–(6) are used with the parameters shown in Table 5. Note that α must be calculated per signal, especially if the signals are not normalized.

Notice in Fig. 8 how the slurry pressure (pump) from test 5 is stable around 2 bar. Noise is filtered out with a low-pass filter of 0.25 Hz. The noise in the pressure signal is outside the healthy range, but is not considered for the curve fitting technique and will need to be characterized separately. The 0.5 confidence threshold of $R^2_{\text{lin,j}}$ from Eq. (6) is based on a 50% likelihood of the window fitting to a linear model. At 50%, the signal is just as likely to be random noise as a linear fit. This

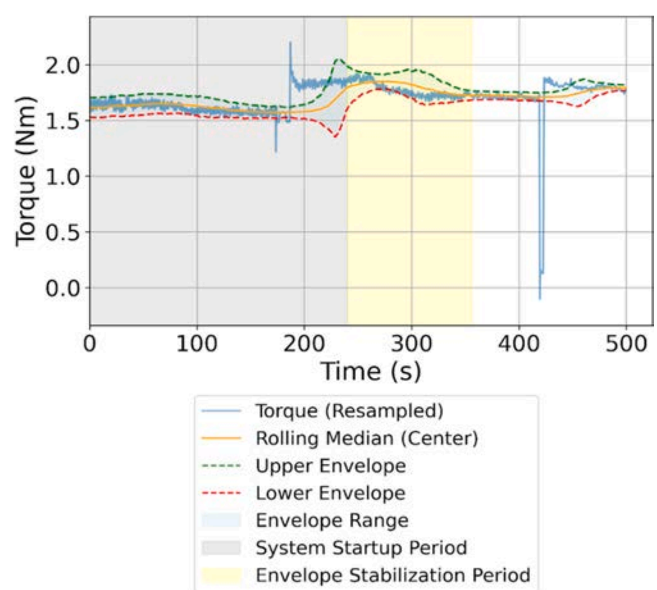

Fig. 7. Median and M.A.D. for Motor Torque (2K mixing head) During Test 7. Median and MAD for head torque using Eqs. (2a) and (2b) with $k = 2.97$ that corresponds to a confidence interval of 95%. During the system startup there is a large envelope breach, which can be ignored at 180 s. Due to the rolling window the envelope requires a period of one full window of 128 s to fully stabilize, which is shown in yellow. At 420 s there is another large envelope breach, which is classified as an anomaly, which corresponds to the 2K mixing head experiencing a leak failure.

loss of confidence in the growth of the slurry pressure (pump) denotes an anomaly and corresponds to poor pumpability of the concrete slurry due to material segregation. Manual detection noticed the anomalous state at 720 s, lagging behind anomalous feature detection, which starts at 490 s.

3.1.5. Magnitude deviation for anomaly detection

Similarly to the confidence in the linear fit in Fig. 8, this detection creates a window using Eq. (4), but only takes into account the slope of

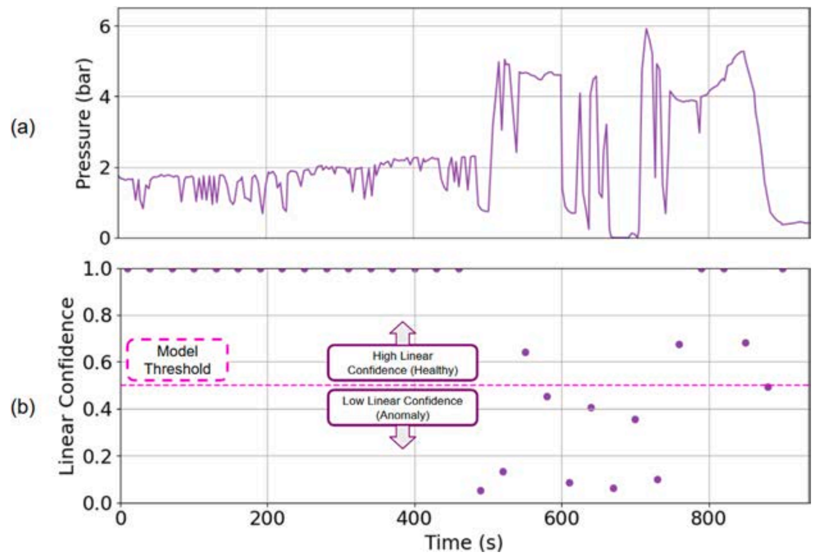

Fig. 8. Linear fit confidence with slurry pressure (Pump). From test 5, the signal of the pressure (a) hovers around 2 bar until material segregation builds enough to hinder pumpability noticeably at 490 s, and observed manually in the extrusion at 720 s. This is detected in (b) using the Eqs. (3)–(6) to generate a fit confidence of the slurry pressure (pump)'s growth rate compared to a linear model shown in Eq. (3). At 490 s the confidence drops below the threshold of 0.5, and is classified as an anomaly.

Table 5
Parameter settings for Eqs. (3)–(6).

Parameter	Value
Window size	6
Window overlap	3
Slope window size	10
Slope window overlap	5
Confidence threshold	0.5
α threshold (pressure)	0.02

Table 6
Parameter settings for Eqs. (3)–(6).

Parameter	Value
Slope window size	50
Slope window overlap	25
α threshold(pressure)	0.02

the linear fit in Eq. (7). The slope α observed in the baseline analysis in Fig. 5 was baselined to be healthy when $|\alpha| < 0.02$. In Fig. 9, the healthy region between -0.02 and 0.02 α is maintained by the slurry pressure (pump) signal from test 5 until 500 s. This technique lags behind the detection shown in curve fitting in Fig. 8, but is still faster than manual detection at 720 s. This technique is comparable to the linear fit confidence but sets a maximum on the growth of a signal, as opposed to the linear fit confidence. It is possible for a near-infinite slope to be represented as a linear model, but in real-world applications there are physical limits (see Table 6).

3.2. Validation: Simulated real-time anomaly detection

After creating and testing the anomalous feature detection models, the system is simulated running real-time anomaly detection with unused data set from tests 8 and 9. These tests are run back-to-back, with a transition in between to change the accelerant which is pumped into the 2K mixing head. This transition leads to a clogging failure in the 2K mixing head. Test 8 exhibits no errors and is considered healthy, and test 9 is an anomalous test that ends in system failure. The frequency-based detection demonstrated in Fig. 6 requires a 128-second window before the first calculation can be made. This is shown in the simulation graphs in Fig. 10. Both tests 8 and 9 are marked as healthy in the manual inspection for the slurry temperature (pump); however, an anomalous feature is detected at 420 s. The operators experienced extrusion problems at 550 s and attempted to fix these issues by injecting more water into the slurry. This minor correction allows the system to continue to function until 650 s, when the 2K mixing head becomes completely clogged. Although the temperature sensor is located near the slurry pump, the disruption in the concrete slurry from 5 m away is still detectable through an increase in noise in the temperature sensor.

Similarly, linear slope-based anomaly detection successfully identifies abnormal growth in the slurry pressure (pump) signal during test 9. As demonstrated in Fig. 8 subplot (b), the signal remains steady throughout test 8, yet never stabilizes during the transition and implementation of test 9. The subtle yet continuous upward trend that occurs after the transition is captured by the slope α calculated across overlapping windows. At approximately 440 s, the slope exceeds the predefined upper threshold of anomalous feature detection of $+0.02$, triggering the first anomalous feature detection (blue line). This precedes the first manual operator detection at 550 s (orange line) and happens well before the critical system failure at 650 s (red line). The results demonstrate that real-time anomaly detection is sensitive enough to identify anomalous pressure changes that are not immediately visible to humans. This suggests that linear slope analysis can serve as a reliable indicator of performance degradation, providing critical intervention time.

Figs. 10–11 show case two examples, namely magnitude deviation for pressure and frequency analysis for temperature, used in detection. The full results of all detections for all tests are shown in Table 7. Across the different validation tests, which were conducted with every signal against every detection technique, the detection methods showed consistent performance in identifying early indicators of system degradation. These modes of degradation were slurry pipeline clogging, material segregation, and slurry mixing anomalies. Test 1 showed that detections were consistent across all methods with the exception of frequency-based torque analysis. This failed to produce reliable outputs due to limited data availability and down-sampled resolution. In Test 2, all monitored signals exhibited at least one anomalous feature, indicating the system's anomalous state.

Test 4 presented a notable discrepancy versus the manual inspection which classified the system as healthy. Yet multiple anomalous features

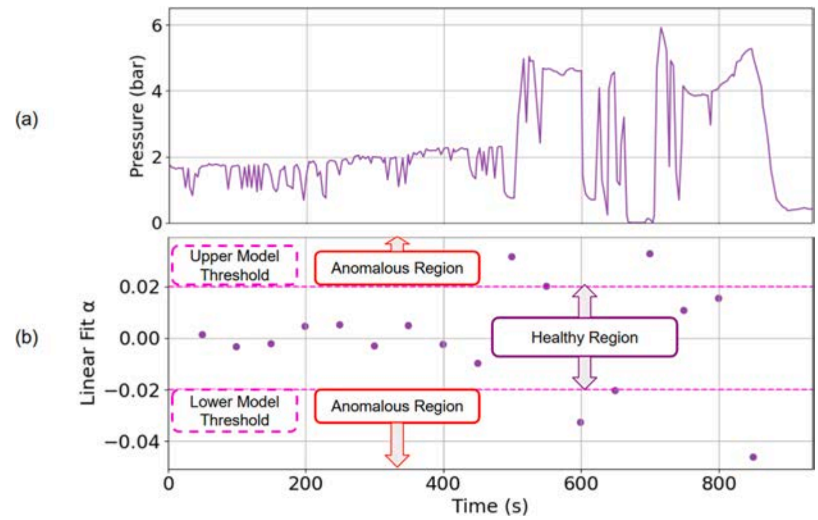

Fig. 9. Magnitude deviation with slurry pressure (Pump). Similar to 8, the slurry pressure (pump) from test 5 breaks the threshold of $|\alpha| > 2$ starting at 500 s. Points past the upper and lower model thresholds are considered anomalous.

Table 7
Anomalous feature detection results.

Test ID	Motor Power (Pump)				Slurry Pressure (Pump)				Slurry Temperature (Pump)				Motor Torque (2K Head)			
	FA	AE	CF	MD	FA	AE	CF	MD	FA	AE	CF	MD	FA	AE	CF	MD
1	H	H	H	H	H	H	H	H	H	H	H	H	A	H	H	H
2	A	A	A	A	H	H	A	A	A	A	H	H	N/A	N/A	N/A	N/A
3	A	A	A	H	H	A	A	A	A	A	H	H	N/A	N/A	N/A	N/A
4	A	H	A	H	A	A	H	H	H	H	H	H	N/A	N/A	N/A	N/A
5	A	A	A	A	A	A	A	A	A	A	H	H	N/A	N/A	N/A	N/A
6	H	A	H	A	A	H	A	A	A	H	H	H	A	A	A	A
7	H	H	H	H	H	A	H	A	H	A	H	H	A	A	A	H
8	H	H	H	H	H	H	H	H	H	H	H	H	A	H	H	H
9	A	A	A	A	A	A	A	A	A	A	H	H	A	A	A	A

N/A - The signal was unable to be recorded.

* Used only for model validation

A=Anomalous
H=Healthy
FA=Frequency Analysis
AE=Amplitude Envelope
CF=Curve Fitting
MD=Magnitude Deviation

RED Red notes a mismatch between manual and automated classification

were identified across distinct signals. Post-analysis of the printed structure, and operator notes of excess sand in the hopper during cleaning, suggest these features may reflect early-stage segregation behavior that did not manifest visibly during operation. This observation underscores a research gap in classifying process deviations, in terms of severity and type, which could amplify the effect of this framework.

Compared to other signals, slurry pressure and slurry temperature were able to provide high-confidence detections. Torque and power signals were more vulnerable to noise and bias. These findings validate the framework's capability to extract meaningful indicators from heterogeneous sensor data which and targeted signal analysis of these indicators can detect anomalies with a higher sensitivity than manual observation. Future enhancements should focus on signal pre-processing and integrating classification modules in preparation for closed loop process control.

While these examples were able to demonstrate that this framework has the potential to identify anomalous behavior earlier than manual detection, this study alone is not enough to characterize warning times or the methodology to do so. A more rigorous analysis will be performed as a larger dataset becomes available.

4. Conclusion

Current 3D concrete printing (3DCP) workflows rely heavily on manual oversight and heuristic adjustments, limiting the ability to detect failures in advance. This constraint forces operators to favor conservative geometries and maintain close supervision, which becomes increasingly impractical as the scale and complexity of fabrication grow. This work introduces a structured anomaly detection framework designed to improve system awareness and responsiveness within the 3DCP workflow.

4.1. Summary of contributions

The presented framework integrates heterogeneous inline sensing with four complementary signal-analysis techniques — frequency analysis, amplitude envelope detection, curve fitting, and magnitude deviation — to extract features linked to system-level degradation. Applied across nine robotic printing experiments, these methods identified early indicators of pump clogging, material segregation, and mixing-head obstruction. In multiple cases, detections occurred well before manual observation or visible defects, including the identification of a previously unlabeled deviation. These findings demonstrate improved

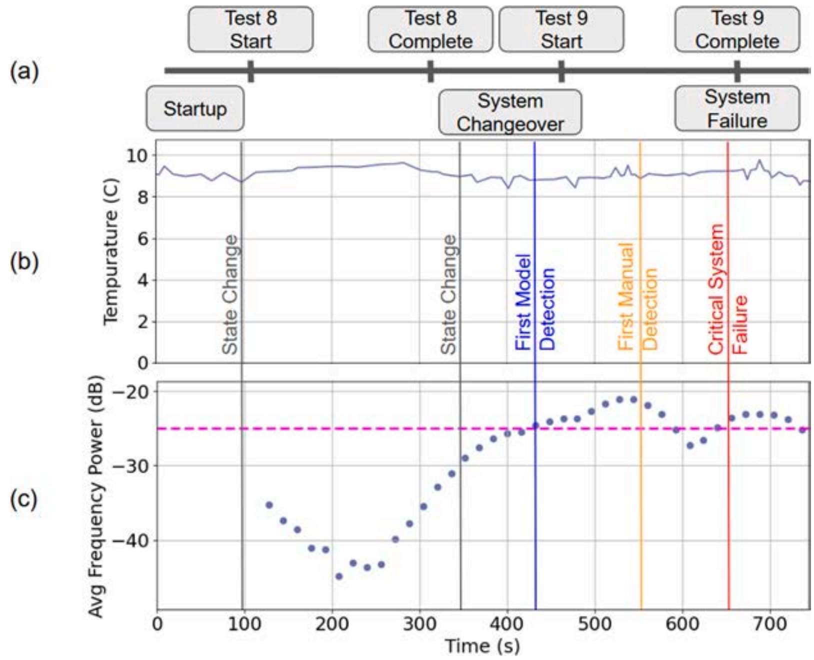

Fig. 10. Verification of frequency detection critical feature: (a) Timeline of experimental events for series of tests 8 and 9 to include system startup, transition period between tests, and ultimately system failure. (b) Slurry pump signature is stable through test 8. Though difficult to see in the raw temperature signal, (c) shows the avg. power of the frequency range from −0.05 to −0.25 dB increases past the −25 dB threshold into anomalous territory at 420 s. There is a problem with the extrusion starting at 550 s, which is documented as the first manual detection. There is a minor water injection rate correction at 550 s, but it is not sufficient enough to prevent system failure at 650 s.

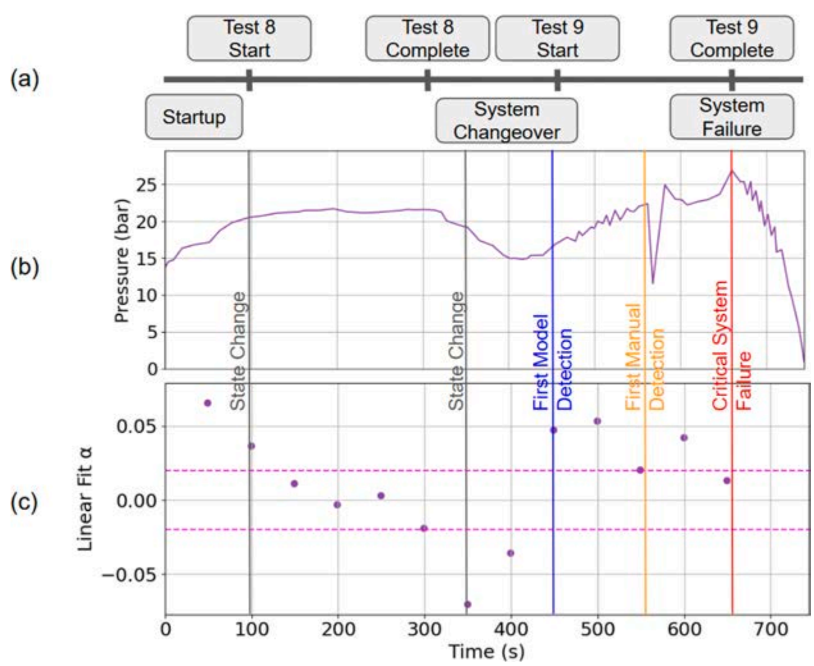

Fig. 11. Real-time detection of pressure anomalies using linear slope thresholding: (a) Timeline of operational phases across tests 8 and 9, including startup, system transition, and final system failure. (b) Slurry pressure (pump) remains relatively stable during test 8, but exhibits gradual growth and sudden fluctuations during test 9. (c) Linear fit slope (α) calculated using a sliding windows approach as defined in Section 3.1.4. Values are flagged as anomalous once $|\alpha|$ exceeds the absolute value of ± 0.02 threshold (dashed magenta lines). The anomalous feature detects abnormal pressure growth starting at 440 s (blue line), preceding manual observation at 550 s (orange) and full system failure at 650 s (red). This method captures early deviations in material flow characteristics linked to system instability.

sensitivity to early-stage disturbances and show that inline process measurements can serve as quantifiable health indicators for pump behavior, material consistency, and mixing performance.

To support transparency and reproducibility, all time aligned system-level data used in this work are publicly available [163].

4.2. Novel components of this work

The distinct contributions of this study are summarized as follows:

- A generalizable system-level methodology that evaluates anomalous behavior for the process of the extrusion system.
- A multimodal feature extraction pipeline enabling robust early-warning detection of both gradual and abrupt degradation.
- A publicly available multi-sensor 2K 3DCP dataset enabling reproducibility and continued research into health-aware automation of concrete AM.
- Experimental evidence that inline signals can reveal latent process risks not visible during printing.

Together, these contributions represent a step toward proactive, data-driven monitoring that improves process reliability and supports first-time-right digital fabrication.

4.3. Future work and outlook

While this study demonstrates reliable detection of evolving anomalies, linking each anomaly type to final construct performance remains an open challenge. Some disturbances (e.g., clogs) directly influence extrusion continuity, whereas others (e.g., mild segregation) may not appear during fabrication but can still affect mechanical performance in the hardened structure.

Future work will focus on:

- Automated and data-driven threshold tuning for improved generalizability across materials, environments, and hardware configurations
- Classification of anomaly types and severity levels related to print outcomes
- Integration of monitoring feedback with real-time control systems for autonomous corrective action

By reducing dependence on manual heuristics and enabling earlier, data-supported intervention, this framework lays foundational capabilities for predictive and autonomous 3DCP operations.

CRediT authorship contribution statement

Abdallah Kamhawi: Writing – review & editing, Writing – original draft, Visualization, Validation, Software, Resources, Methodology, Investigation, Formal analysis, Data curation, Conceptualization. **Yuxin Lin:** Writing – review & editing, Writing – original draft, Visualization, Validation, Software, Resources, Methodology, Investigation, Formal analysis, Data curation, Conceptualization. **Christopher Watson:** Writing – review & editing, Writing – original draft, Visualization, Validation, Software, Resources, Methodology, Investigation, Formal analysis, Data curation, Conceptualization. **Kira Barton:** Writing – review & editing, Writing – original draft, Supervision, Resources, Project administration, Funding acquisition, Conceptualization. **Mania Aghaei Meibodi:** Writing – review & editing, Writing – original draft, Supervision, Resources, Project administration, Funding acquisition, Conceptualization.

Funding

This work was supported by the Taubman College of Architecture Pressing Matters initiative, the Michigan Materials Research Institute, the Rackham Merit Fellowship Program, and the Sika Corporation.

Declaration of competing interest

The authors declare that they have no known competing financial interests or personal relationships that could have appeared to influence the work reported in this paper.

Data availability

The data is made available at https://doi.org/10.5281/zenodo.17308420.

References

[1] R.A. Buswell, W.L. Da Silva, F.P. Bos, H. Schipper, D. Lowke, N. Hack, H. Kloft, V. Mechtcherine, T. Wangler, N. Roussel, A process classification framework for defining and describing Digital Fabrication with Concrete, Cem. Concr. Res. 134 (2020) 106068.
[2] A. Kamhawi, M.A. Meibodi, Techniques and strategies in extrusion based 3D concrete printing of complex components to prevent premature failure, Autom. Constr. 168 (2024) 105768.
[3] A. Kamhawi, J. Brown, A. Fahmy, M. Aghaei Meibodi, Waste-free production of ultra-thin concrete panels via robotic 3D printing and CNC dynamic bed device, in: RILEM International Conference on Concrete and Digital Fabrication, Springer, 2024, pp. 99–106.
[4] F. Hamidi, F. Aslani, Additive manufacturing of cementitious composites: Materials, methods, potentials, and challenges, Constr. Build. Mater. 218 (2019) 582–609.
[5] A. Anton, P. Bedarf, A. Yoo, B. Dillenburger, L. Reiter, T. Wangler, R.J. Flatt, Concrete choreography: prefabrication of 3D-printed columns, in: Fabricate 2020: Making Resilient Architecture, UCL Press, 2020, pp. 286–293.
[6] Y. Chen, S. He, Y. Gan, O. Çopuroğlu, F. Veer, E. Schlangen, A review of printing strategies, sustainable cementitious materials and characterization methods in the context of extrusion-based 3D concrete printing, J. Build. Eng. 45 (2022) 103599.
[7] F. Bos, R. Wolfs, Z. Ahmed, T. Salet, Additive manufacturing of concrete in construction: potentials and challenges of 3D concrete printing, Virtual Phys. Prototyp. 11 (3) (2016) 209–225.
[8] C. Menna, J. Mata-Falcón, F.P. Bos, G. Vantyghem, L. Ferrara, D. Asprone, T. Salet, W. Kaufmann, Opportunities and challenges for structural engineering of digitally fabricated concrete, Cem. Concr. Res. 133 (2020) 106079.
[9] Y. Lin, A. Bayramvand, M. Aghaei Meibodi, Towards lightweight structure: Coupling topology optimization with non-planar 3D concrete printing, in: H. Chai, D.W.N. Bao, Z. Guo, P.F. Yuan (Eds.), Symbiotic Intelligence, Springer Nature Singapore, Singapore, 2025, pp. 3–12.
[10] R. Wolfs, D. Bos, J.-F. Caron, M. Gerke, R. Mesnil, R. Buswell, N. Ducoulombier, N. Hack, E. Keita, P. Kinnell, et al., On-line and in-line quality assessment across all scale levels of 3D concrete printing, Cem. Concr. Res. 185 (2024) 107646.
[11] F. Bos, R. Wolfs, Z. Ahmed, T. Salet, Large scale testing of digitally fabricated concrete (DFC) elements, in: First RILEM International Conference on Concrete and Digital Fabrication–Digital Concrete 2018, Springer, 2019, pp. 129–147.
[12] Z.Y. Ahmed, R.J. Wolfs, F.P. Bos, T.A. Salet, A framework for large-scale structural applications of 3D printed concrete: the case of a 29 m bridge in the Netherlands, in: Open Conference Proceedings, Vol. 1, TIB Open Publishing (Technische Informationsbibliothek), 2022, pp. 5–19.
[13] R. Wolfs, D. Bos, T. Salet, Lessons learned of project Milestone: The first 3D printed concrete house in the Netherlands, Mater. Today: Proc. (2023).
[14] M.A. Meibodi, Y. Lin, H. Chen, Hybrid approaches towards 3D concrete printing for lightweight reinforced concrete structures, in: D. Lowke, N. Freund, D. Böhler, F. Herding (Eds.), Digital Concrete 2024 - Supplementary Proceedings, Braunschweig, 2024, http://dx.doi.org/10.24355/dbbs.084-202408140649-0, URL https://leopard.tu-braunschweig.de/receive/dbbs_mods_00077799.
[15] T. Ooms, G. Vantyghem, R. Van Coile, W. De Corte, A parametric modelling strategy for the numerical simulation of 3D concrete printing with complex geometries, Addit. Manuf. 38 (2021) 101743.
[16] Y. Tao, K. Lesage, K. Van Tittelboom, Y. Yuan, G. De Schutter, Twin-pipe pumping strategy for stiffening control of 3D printable concrete: From transportation to fabrication, Cem. Concr. Res. 168 (2023) 107137.
[17] V. Mechtcherine, F.P. Bos, A. Perrot, W.L. Da Silva, V. Nerella, S. Fataei, R.J. Wolfs, M. Sonebi, N. Roussel, Extrusion-based additive manufacturing with cement-based materials–production steps, processes, and their underlying physics: a review, Cem. Concr. Res. 132 (2020) 106037.
[18] N. Roussel, Rheological requirements for printable concretes, Cem. Concr. Res. 112 (2018) 76–85.
[19] J. Kruger, S. Zeranka, G. van Zijl, 3D concrete printing: A lower bound analytical model for buildability performance quantification, Autom. Constr. 106 (2019) 102904.

[20] R.A. Buswell, W.L. De Silva, S.Z. Jones, J. Dirrenberger, 3D printing using concrete extrusion: A roadmap for research, Cem. Concr. Res. 112 (2018) 37–49.
[21] Y. Tao, A. Rahul, K. Lesage, Y. Yuan, K. Van Tittelboom, G. De Schutter, Stiffening control of cement-based materials using accelerators in inline mixing processes: possibilities and challenges, Cem. Concr. Compos. 119 (2021) 103972.
[22] Y.W.D. Tay, M.Y. Li, M.J. Tan, Effect of printing parameters in 3D concrete printing: Printing region and support structures, J. Mater. Process. Technol. 271 (2019) 261–270.
[23] T. Dorn, O. Blask, D. Stephan, Acceleration of cement hydration–A review of the working mechanisms, effects on setting time, and compressive strength development of accelerating admixtures, Constr. Build. Mater. 323 (2022) 126554.
[24] Y. Tao, A. Rahul, K. Lesage, K. Van Tittelboom, Y. Yuan, G. De Schutter, Mechanical and microstructural properties of 3D printable concrete in the context of the twin-pipe pumping strategy, Cem. Concr. Compos. 125 (2022) 104324.
[25] W. De Corte, G. Vantyghem, T. Ooms, Strategies for numerical simulation of 3D concrete printing : voxel-based versus extrusion-based meshing, in: E. Júlio, J. Valença, A.S. Louro (Eds.), Concrete Structure : New Trends for Eco-Efficiency and Performance, no. 54, 2021, p. 10.
[26] G. Vantyghem, T. Ooms, W. De Corte, VoxelPrint: A Grasshopper plug-in for voxel-based numerical simulation of concrete printing, Autom. Constr. 122 (2021) 103469.
[27] A.S. Suiker, R.J. Wolfs, S.M. Lucas, T.A. Salet, Elastic buckling and plastic collapse during 3D concrete printing, Cem. Concr. Res. 135 (2020) 106016.
[28] F.P. Bos, C. Menna, M. Pradena, E. Kreiger, W.L. da Silva, A.U. Rehman, D. Weger, R. Wolfs, Y. Zhang, L. Ferrara, et al., The realities of additively manufactured concrete structures in practice, Cem. Concr. Res. 156 (2022) 106746.
[29] G. Ma, R. Buswell, W.R.L. da Silva, L. Wang, J. Xu, S.Z. Jones, Technology readiness: A global snapshot of 3D concrete printing and the frontiers for development, Cem. Concr. Res. 156 (2022) 106774.
[30] R. Buswell, J. Xu, D. De Becker, J. Dobrzanski, J. Provis, J.T. Kolawole, P. Kinnell, Geometric quality assurance for 3D concrete printing and hybrid construction manufacturing using a standardised test part for benchmarking capability, Cem. Concr. Res. 156 (2022) 106773.
[31] U. Boddepalli, B. Panda, I.S. Ranjani Gandhi, Rheology and printability of Portland cement based materials: a review, J. Sustain. Cem.-Based Mater. 12 (7) (2023) 789–807.
[32] B.M. Birru, A.U. Rehman, J.-H. Kim, Comparative analysis of structural build-up in one-component stiff and two-component shotcrete-accelerated set-on-demand mixtures for 3D concrete printing, Virtual Phys. Prototyp. 19 (1) (2024) e2359625.
[33] L. Lima, T. Wangler, A.M. Sanchez, A. Anton, R.J. Flatt, Durability of 3D printed concrete: Performance assessment of a two-component system against water absorption, carbonation, and chloride ingress, in: D. Lowke, N. Freund, D. Böhler, F. Herding (Eds.), Fourth RILEM International Conference on Concrete and Digital Fabrication, Springer Nature Switzerland, Cham, 2024, pp. 291–298.
[34] T. Wangler, Y. Tao, A. Das, M. Mahmoudi, S. Gürel, R.J. Flatt, Aluminate 2K systems in digital concrete: Process, design, chemistry, and outlook, Cem. Concr. Res. 185 (2024) 107644, http://dx.doi.org/10.1016/j.cemconres.2024.107644, URL https://www.sciencedirect.com/science/article/pii/S0008884624002254.
[35] A.U. Rehman, A. Perrot, B.M. Birru, J.-H. Kim, Recommendations for quality control in industrial 3D concrete printing construction with mono-component concrete: a critical evaluation of ten test methods and the introduction of the performance index, Dev. Built Environ. 16 (2023) 100232.
[36] R.J. Flatt, T. Wangler, On sustainability and digital fabrication with concrete, Cem. Concr. Res. 158 (2022) 106837.
[37] L. Reiter, T. Wangler, A. Anton, R.J. Flatt, Setting on demand for digital concrete–Principles, measurements, chemistry, validation, Cem. Concr. Res. 132 (2020) 106047.
[38] A.-M. Anton, Tectonics of Concrete Printed Architecture: Technology, Components and Assemblies for Column-Slab Construction (Ph.D. thesis), ETH Zurich, 2022.
[39] M. Dahlenburg, C.M. Hechtl, C. Matthäus, J. Fottner, 3D-concrete printing–graded concrete extrusion, in: 2022 3rd International Conference on Computation, Automation and Knowledge Management, ICCAKM, IEEE, 2022, pp. 1–5.
[40] T. Wangler, R. Pileggi, S. Gürel, R.J. Flatt, A chemical process engineering look at digital concrete processes: critical step design, inline mixing, and scaleup, Cem. Concr. Res. 155 (2022) 106782.
[41] D.H. Bos, R.J. Wolfs, A quality control framework for digital fabrication with concrete, RILEM Tech. Lett. 8 (2023) 106–112.
[42] V. Mechtcherine, K. Van Tittelboom, A. Kazemian, E. Kreiger, B. Nematollahi, V.N. Nerella, M. Santhanam, G. De Schutter, G. Van Zijl, D. Lowke, et al., A roadmap for quality control of hardening and hardened printed concrete, Cem. Concr. Res. 157 (2022) 106800.
[43] D. Chopin, B. Cazacliu, F.d. Larrard, R.d. Schell, Monitoring of concrete homogenisation with the power consumption curve, Mater. Struct. 40 (2007) 897–907.
[44] B. Cazacliu, N. Roquet, Concrete mixing kinetics by means of power measurement, Cem. Concr. Res. 39 (3) (2009) 182–194.
[45] J. Versteege, R. Wolfs, T. Salet, Data-driven additive manufacturing with concrete: Enhancing in-line sensory data with domain knowledge, Part II: Moisture and heat, Autom. Constr. 177 (2025) 106327, http://dx.doi.org/10.1016/j.autcon.2025.106327, URL https://www.sciencedirect.com/science/article/pii/S092658052500367X.
[46] C. Astm, 1074-04, Standard practice for estimating concrete strength by the maturity method, ASTM Stand. 4 (2004).
[47] K. Mawas, M. Maboudi, M. Gerke, Automatic geometric inspection in digital fabrication, Int. Arch. Photogramm. Remote Sens. Spat. Inf. Sci. 43 (2022) 459–466.
[48] S. Zimmermann, D. Griego, R.J. Flatt, Visualizing defects of concrete 3D printed structures with augmented reality based on machine learning-driven image analysis, in: RILEM International Conference on Concrete and Digital Fabrication, Springer, 2024, pp. 150–157.
[49] C. Gill, L. Justham, N. Lohse, A. Haynes, J. Dobrzanski, R. Buswell, P. Kinnell, Measurement and control of serial manipulator robots for 3D concrete printing, in: RILEM International Conference on Concrete and Digital Fabrication, Springer, 2024, pp. 91–98.
[50] N. Ashrafi, S. Nazarian, N.A. Meisel, J.P. Duarte, Experimental prediction of material deformation in large-scale additive manufacturing of concrete, Addit. Manuf. 37 (2021) 101656.
[51] Y. Lin, M. Aghaei Meibodi, Integrated sensing printhead: In-line data collection for non-planar 3D concrete printing, in: A. Nahmad-Vazquez, J. Johnson, J. Taron, J. Rhee, D. Hapton (Eds.), Proceedings of the 44th Annual Conference for the Association for Computer Aided Design in Architecture (ACADIA 2024: Designing Change), Vol. 2, 2024, pp. 355–364.
[52] J. Versteege, R. Wolfs, T. Salet, Data-driven additive manufacturing with concrete: Enhancing in-line sensory data with domain knowledge, Part I: Geometry, Autom. Constr. 172 (2025) 106020, http://dx.doi.org/10.1016/j.autcon.2025.106020, URL https://www.sciencedirect.com/science/article/pii/S0926580525000603.
[53] A. Oleff, B. Küster, M. Stonis, L. Overmeyer, Process monitoring for material extrusion additive manufacturing: a state-of-the-art review, Prog. Addit. Manuf. 6 (2021) 705–730, URL https://doi.org/10.1007/s40964-021-00192-4.
[54] L. Li, R. McGuan, R. Isaac, P. Kavehpour, R. Candler, Improving precision of material extrusion 3D printing by in-situ monitoring & predicting 3D geometric deviation using conditional adversarial networks, Addit. Manuf. 38 (2021) 101695.
[55] P. Farrokhsiar, B. Gursoy, J.P. Duarte, A comprehensive review on integrating vision-based sensing in extrusion-based 3D printing processes: toward geometric monitoring of extrusion-based 3D concrete printing, Constr. Robot. 8 (2) (2024) 21.
[56] J. Xu, R.A. Buswell, P. Kinnell, I. Biro, J. Hodgson, N. Konstantinidis, L. Ding, Inspecting manufacturing precision of 3D printed concrete parts based on geometric dimensioning and tolerancing, Autom. Constr. 117 (2020) 103233.
[57] R. Rill-García, E. Dokladalova, P. Dokládal, J.-F. Caron, R. Mesnil, P. Margerit, M. Charrier, Inline monitoring of 3D concrete printing using computer vision, Addit. Manuf. 60 (2022) 103175.
[58] S. Senthilnathan, B. Raphael, Using computer vision for monitoring the quality of 3d-printed concrete structures, Sustainability 14 (23) (2022) 15682.
[59] S. Garfo, M. Muktadir, S. Yi, Defect detection on 3d print products and in concrete structures using image processing and convolution neural network, J. Mechatron. Robot. 4 (1) (2020) 74–84.
[60] O. Davtalab, A. Kazemian, X. Yuan, B. Khoshnevis, Automated inspection in robotic additive manufacturing using deep learning for layer deformation detection, J. Intell. Manuf. 33 (3) (2022) 771–784.
[61] A. Kazemian, X. Yuan, O. Davtalab, B. Khoshnevis, Computer vision for real-time extrusion quality monitoring and control in robotic construction, Autom. Constr. 101 (2019) 92–98.
[62] C. Liu, A.C.C. Law, D. Roberson, Z.J. Kong, Image analysis-based closed loop quality control for additive manufacturing with fused filament fabrication, J. Manuf. Syst. 51 (2019) 75–86, http://dx.doi.org/10.1016/j.jmsy.2019.04.002, URL https://www.sciencedirect.com/science/article/pii/S0278612518304060.
[63] T. Huang, S. Wang, S. Yang, W. Dai, Statistical process monitoring in a specified period for the image data of fused deposition modeling parts with consistent layers, J. Intell. Manuf. 32 (2021) 2181–2196.
[64] K. He, Q. Zhang, Y. Hong, Profile monitoring based quality control method for fused deposition modeling process, J. Intell. Manuf. 30 (2) (2019) 947–958.
[65] F. Baumann, D. Roller, Vision based error detection for 3D printing processes, in: MATEC Web of Conferences, Vol. 59, EDP Sciences, 2016, p. 06003.
[66] Y. Chen, Y. Zhang, Z. Liu, W. Zhang, B. Pang, Y. Zhang, D. Wang, Quantitative surface quality evaluation for 3D-printed concrete with coarse aggregate through 3D scanning, Case Stud. Constr. Mater. 20 (2024) e03077.
[67] K. Mawas, M. Maboudi, M. Gerke, Filament extraction in 3D printing of shotcrete walls from terrestrial laser scanner data, Int. Arch. Photogramm. Remote Sens. Spat. Inf. Sci. 48 (2023) 307–313.

[68] X. Zhao, Q. Lian, Z. He, S. Zhang, Region-based online flaw detection of 3D printing via fringe projection, Meas. Sci. Technol. 31 (3) (2019) 035011.
[69] O. Holzmond, X. Li, In situ real time defect detection of 3D printed parts, Addit. Manuf. 17 (2017) 135–142.
[70] J. Jhun, D.-H. Lee, A. Ur Rehman, S. Kang, J.-H. Kim, Development of a real-time geometric quality monitoring system for extruded filaments of 3D concrete printing construction, IEEE Access 12 (2024) 69981–69999, http://dx.doi.org/10.1109/ACCESS.2024.3401472.
[71] W. Lin, H. Shen, J. Fu, S. Wu, Online quality monitoring in material extrusion additive manufacturing processes based on laser scanning technology, Precis. Eng. 60 (2019) 76–84.
[72] O.A. Jeyifous, E. Schönsee, C. Strangfeld, G. Hüsken, Correlation of continuously measured in-line process parameters and extruded geometry in 3D concrete printing experiments, in: RILEM International Conference on Concrete and Digital Fabrication, Springer, 2024, pp. 127–133.
[73] T.K.N. Quah, Y.W.D. Tay, J.H. Lim, M.J. Tan, T.N. Wong, K.H.H. Li, Concrete 3D printing: process parameters for process control, monitoring and diagnosis in automation and construction, Mathematics 11 (6) (2023) 1499.
[74] The BOB2, 2025, (Accessed 27 September 2025). URL https://cobod.com/solution/bod2/.
[75] Rapid hardening for complex designs, 2025, (Accessed 27 September 2025). URL https://www.vertico.com/printhead/accelerator.
[76] ICON's next-gen multi-story construction system, 2025, (Accessed: 2025-09-27). URL https://iconbuild.com/robotics.
[77] R. Comminal, W.R.L. da Silva, T.J. Andersen, H. Stang, J. Spangenberg, Modelling of 3D concrete printing based on computational fluid dynamics, Cem. Concr. Res. 138 (2020) 106256.
[78] A. Perrot, A. Pierre, V. Nerella, R. Wolfs, E. Keita, S. Nair, N. Neithalath, N. Roussel, V. Mechtcherine, From analytical methods to numerical simulations: A process engineering toolbox for 3D concrete printing, Cem. Concr. Compos. 122 (2021) 104164.
[79] A. Baktheer, M. Classen, A review of recent trends and challenges in numerical modeling of the anisotropic behavior of hardened 3D printed concrete, Addit. Manuf. (2024) 104309.
[80] V. Nguyen-Van, S. Li, J. Liu, K. Nguyen, P. Tran, Modelling of 3D concrete printing process: A perspective on material and structural simulations, Addit. Manuf. 61 (2023) 103333.
[81] R. Wolfs, F.P. Bos, T. Salet, Early age mechanical behaviour of 3D printed concrete: Numerical modelling and experimental testing, Cem. Concr. Res. 106 (2018) 103–116.
[82] W. Zhao, J.P. Queralta, T. Westerlund, Sim-to-real transfer in deep reinforcement learning for robotics: a survey, in: 2020 IEEE Symposium Series on Computational Intelligence, SSCI, 2020, pp. 737–744, http://dx.doi.org/10.1109/SSCI47803.2020.9308468.
[83] E. Salvato, G. Fenu, E. Medvet, F.A. Pellegrino, Crossing the reality gap: A survey on sim-to-real transferability of robot controllers in reinforcement learning, IEEE Access 9 (2021) 153171–153187, http://dx.doi.org/10.1109/ACCESS.2021.3126658.
[84] X.B. Peng, M. Andrychowicz, W. Zaremba, P. Abbeel, Sim-to-real transfer of robotic control with dynamics randomization, in: 2018 IEEE International Conference on Robotics and Automation, ICRA, IEEE, 2018, pp. 3803–3810.
[85] J. Tan, T. Zhang, E. Coumans, A. Iscen, Y. Bai, D. Hafner, S. Bohez, V. Vanhoucke, Sim-to-real: Learning agile locomotion for quadruped robots, 2018, arXiv preprint arXiv:1804.10332.
[86] MAI® MULTIMIX-3D: Precision and innovation in 3D concrete printing, 2025, (Accessed 12 January 2025). URL https://mai.at/en/product-range/3d-printing/mai-multimix-3d.
[87] J. Klespitz, L. Kovács, Peristaltic pumps — A review on working and control possibilities, in: 2014 IEEE 12th International Symposium on Applied Machine Intelligence and Informatics, SAMI, 2014, pp. 191–194, http://dx.doi.org/10.1109/SAMI.2014.6822404.
[88] V. Todorov, B. Aprahamian, H. Tahrilov, Applicability of peristaltic pumps in installations for vegetable oils processing, in: 2016 19th International Symposium on Electrical Apparatus and Technologies, SIELA, 2016, pp. 1–4, http://dx.doi.org/10.1109/SIELA.2016.7543054.
[89] S.C. Gasoto, B. Schneider Jr., J.A. Setti, Study of the pulse of peristaltic pumps for use in 3D extrusion bioprinting, ACS Omega 7 (28) (2022) 24091–24101.
[90] AM8132 | servomotor 2.4 Nm (M_0), F3 (72 mm), 2024, (Accessed 12 January 2025). URL https://www.beckhoff.com/en-us/products/motion/rotary-servomotors/am8100-servomotors-for-compact-drive-technology/am8132.html.
[91] PLE – economy planetary gearbox, 2024, (Accessed 12 January 2025). URL https://www.neugart.com/en-us/gearboxes/economy-gearboxes/ple.
[92] AM8033 servomotor, 2025, URL https://www.beckhoff.com/en-us/products/motion/rotary-servomotors/am8000-servomotors/am8033.html.
[93] KUKA robotics and automation solutions, 2025, (Accessed 12 January 2025). URL https://www.kuka.com/en-us.
[94] General requirements for the competence of testing and calibration laboratories, 2017.
[95] Temperature humidity transmitter, 4-20mA outputs, 2025, https://www.cometsystem.com/products/economy-humidity-and-temperature-transmitter-with-4-20ma-outputs/reg-p3110e, (Accessed 23 March 2025).
[96] WIKA model A-10 pressure sensor, 2025, https://www.wika.com/en-en/a_10.WIKA, (Accessed 23 March 2025).
[97] Yaskawa - PLC and I/O systems, 2025, https://www.yaskawa.eu.com/controls/plc-control-systems, (Accessed 23 March 2025).
[98] DS18b20 datasheet and product info | analog devices, 2025, https://www.analog.com/en/products/ds18b20.html, (Accessed 23 March 2025).
[99] A.A. Almusallam, Effect of environmental conditions on the properties of fresh and hardened concrete, Cem. Concr. Compos. 23 (4–5) (2001) 353–361.
[100] H. Jin, X. Fan, Z. Li, W. Zhang, J. Liu, D. Zhong, L. Tang, An experimental study on the influence of continuous ambient humidity conditions on relative humidity changes, chloride diffusion and microstructure in concrete, J. Build. Eng. 59 (2022) 105112, http://dx.doi.org/10.1016/j.jobe.2022.105112, URL https://www.sciencedirect.com/science/article/pii/S2352710222011202.
[101] Y.G. Jun Zhang, S. Wei, Determination of moisture diffusion coefficient of concrete at early age from interior humidity measurements, Dry. Technol. 29 (6) (2011) 689–696, http://dx.doi.org/10.1080/07373937.2010.528106, URL https://www.tandfonline.com/doi/abs/10.1080/07373937.2010.528106.
[102] D. Shen, C. Liu, M. Wang, X. Jin, H. Tang, Prediction model for internal relative humidity in early-age concrete under different curing humidity conditions, Constr. Build. Mater. 265 (2020) 119987, http://dx.doi.org/10.1016/j.conbuildmat.2020.119987, URL https://www.sciencedirect.com/science/article/pii/S0950061820319929.
[103] M.H. Naser, F.H. Naser, A.H.N. Almamoori, The effect of water mixing temperature on concrete compressive strength containing different ratios of silica fume, IOP Conf. Ser.: Mater. Sci. Eng. 928 (2) (2020) 022010, http://dx.doi.org/10.1088/1757-899X/928/2/022010.
[104] S. Eskandarsefat, Investigation on the effects of mix water temperature on High-Early strength cement concrete properties – An experimental work and a case study, J. Build. Eng. 20 (2018) 208–212, http://dx.doi.org/10.1016/j.jobe.2018.07.023, URL https://www.sciencedirect.com/science/article/pii/S2352710218306685.
[105] A. Tasri, A. Susilawati, Effect of cooling water temperature and space between cooling pipes of post-cooling system on temperature and thermal stress in mass concrete, J. Build. Eng. 24 (2019) 100731, http://dx.doi.org/10.1016/j.jobe.2019.100731, URL https://www.sciencedirect.com/science/article/pii/S2352710217307052.
[106] N. Roussel, C. Lanos, Z. Toutou, Identification of Bingham fluid flow parameters using a simple squeeze test, J. Non-Newton. Fluid Mech. 135 (1) (2006) 1–7, http://dx.doi.org/10.1016/j.jnnfm.2005.12.001, URL https://www.sciencedirect.com/science/article/pii/S0377025705002697.
[107] J. Wiklund, M. Rahman, U. Håkansson, In-line rheometry of micro cement based grouts–A promising new industrial application of the ultrasound based UVP+PD method, Appl. Rheol. 22 (4) (2012) 42783.
[108] E. Buckingham, On plastic flow through capillary tubes, in: Proc. Am. Soc. Testing Materials, 1921, pp. 1154–1156.
[109] V. Nerella, M. Näther, A. Iqbal, M. Butler, V. Mechtcherine, Inline quantification of extrudability of cementitious materials for digital construction, Cem. Concr. Compos. 95 (2019) 260–270, http://dx.doi.org/10.1016/j.cemconcomp.2018.09.015, URL https://www.sciencedirect.com/science/article/pii/S0958946518302956.
[110] S. Taheri, A review on five key sensors for monitoring of concrete structures, Constr. Build. Mater. 204 (2019) 492–509, http://dx.doi.org/10.1016/j.conbuildmat.2019.01.172, URL https://www.sciencedirect.com/science/article/pii/S0950061819302090.
[111] S. Teixeira, A. Santilli, I. Puente, Demoulding vertical elements: Recommendations for apply maturity functions, Constr. Build. Mater. 145 (2017) 392–401, http://dx.doi.org/10.1016/j.conbuildmat.2017.04.006, URL https://www.sciencedirect.com/science/article/pii/S0950061817306451.
[112] B. Kasemsadeh, C. Iascone, Optimizing Placement and Routing for Humidity Sensors, Texas Instruments Incorporated Application Report. SNAA297A-September, 2016.
[113] R. Rill-García, E. Dokladalova, P. Dokládal, J.-F. Caron, R. Mesnil, P. Margerit, M. Charrier, Inline monitoring of 3D concrete printing using computer vision, Addit. Manuf. 60 (2022) 103175, http://dx.doi.org/10.1016/j.addma.2022.103175, URL https://www.sciencedirect.com/science/article/pii/S2214860422005644.
[114] C. Hunt, TCP/IP Network Administration, vol. 2, " O'Reilly Media, Inc.", 2002.
[115] J.R. Moyne, D.M. Tilbury, The emergence of industrial control networks for manufacturing control, diagnostics, and safety data, Proc. IEEE 95 (1) (2007) 29–47, http://dx.doi.org/10.1109/JPROC.2006.887325.
[116] S.-H. Leitner, W. Mahnke, OPC UA – service-oriented architecture for industrial applications, Softwaretechnik-Trends 26 (4) (2006).
[117] D.J. Barrett, R.E. Silverman, SSH, the Secure Shell: The Definitive Guide, " O'Reilly Media, Inc.", 2001.
[118] C. Watson, Eyeballs. URL https://github.com/addsandwich/Eyeballs.
[119] F. Sivrikaya, B. Yener, Time synchronization in sensor networks: a survey, IEEE Netw. 18 (4) (2004) 45–50, http://dx.doi.org/10.1109/MNET.2004.1316761.
[120] T. Bray, The Javascript Object Notation (Json) Data Interchange Format, Tech. rep., Internet Engineering Task Force (IETF), 2014.
[121] P.J. Davis, Interpolation and Approximation, Dover Publications, 2014.

[122] H. Akima, A new method of interpolation and smooth curve fitting based on local procedures, J. ACM 17 (4) (1970) 589–602.
[123] H. Akima, A method of bivariate interpolation and smooth surface fitting based on local procedures, Commun. ACM 17 (1) (1974) 18–20.
[124] R.G. Lyons, Understanding Digital Signal Processing, 3/E, Pearson Education India, 1997.
[125] J. Needham, Science and Civilisation in China, vol. 5, Cambridge University Press, 1974.
[126] P. Thévenaz, T. Blu, M. Unser, Image interpolation and resampling, Handb. Med. Imaging Process. Anal. 1 (1) (2000) 393–420.
[127] S.K. Mitra, Digital Signal Processing: A Computer-Based Approach, vol. 2, McGraw-Hill, New York, NY, USA, 2011.
[128] F. Harris, On the use of windows for harmonic analysis with the discrete Fourier transform, Proc. IEEE 66 (1) (1978) 51–83, http://dx.doi.org/10.1109/PROC.1978.10837.
[129] M.W. Trethewey, Window and overlap processing effects on power estimates from spectra, Mech. Syst. Signal Process. 14 (2) (2000) 267–278.
[130] V.C.M.N. Leite, J.G. Borges da Silva, G.F.C. Veloso, L.E. Borges da Silva, G. Lambert-Torres, E.L. Bonaldi, L.E. de Lacerda de Oliveira, Detection of localized bearing faults in induction machines by spectral kurtosis and envelope analysis of stator current, IEEE Trans. Ind. Electron. 62 (3) (2015) 1855–1865, http://dx.doi.org/10.1109/TIE.2014.2345330.
[131] T. Barszcz, A. JabŁoński, A novel method for the optimal band selection for vibration signal demodulation and comparison with the Kurtogram, Mech. Syst. Signal Process. 25 (1) (2011) 431–451.
[132] P.W. Tse, Y. Peng, R. Yam, Wavelet analysis and envelope detection for rolling element bearing fault diagnosis—their effectiveness and flexibilities, J. Vib. Acoust. 123 (3) (2001) 303–310.
[133] J. Antoni, The spectral kurtosis: a useful tool for characterising non-stationary signals, Mech. Syst. Signal Process. 20 (2) (2006) 282–307.
[134] J. Antoni, R.B. Randall, The spectral kurtosis: application to the vibratory surveillance and diagnostics of rotating machines, Mech. Syst. Signal Process. 20 (2) (2006) 308–331.
[135] M. Farge, et al., Wavelet transforms and their applications to turbulence, Annu. Rev. Fluid Mech. 24 (1) (1992) 395–458.
[136] P.P. Vaidyanathan, Multirate digital filters, filter banks, polyphase networks, and applications: a tutorial, Proc. IEEE 78 (1) (1990) 56–93.
[137] H. Landau, Sampling, data transmission, and the Nyquist rate, Proc. IEEE 55 (10) (1967) 1701–1706.
[138] H. Nolan, R. Whelan, R.B. Reilly, FASTER: fully automated statistical thresholding for EEG artifact rejection, J. Neurosci. Methods 192 (1) (2010) 152–162.
[139] C. Leys, C. Ley, O. Klein, P. Bernard, L. Licata, Detecting outliers: Do not use standard deviation around the mean, use absolute deviation around the median, J. Exp. Soc. Psychol. 49 (4) (2013) 764–766, http://dx.doi.org/10.1016/j.jesp.2013.03.013, URL https://www.sciencedirect.com/science/article/pii/S0022103113000668.
[140] W. Maddams, The scope and limitations of curve fitting, Appl. Spectrosc. 34 (3) (1980) 245–267.
[141] W. Rudin, Real and Complex Analysis: 3rd. Ed., McGraw-Hill, 1987.
[142] M. Rosenblatt, Curve estimates, Ann. Math. Stat. 42 (6) (1971) 1815–1842.
[143] F.R. Hampel, The influence curve and its role in robust estimation, J. Amer. Statist. Assoc. 69 (346) (1974) 383–393.
[144] X. Jin, Y. Sun, Z. Que, Y. Wang, T.W.S. Chow, Anomaly detection and fault prognosis for bearings, IEEE Trans. Instrum. Meas. 65 (9) (2016) 2046–2054, http://dx.doi.org/10.1109/TIM.2016.2570398.
[145] M. Desforges, P. Jacob, J. Cooper, Applications of probability density estimation to the detection of abnormal conditions in engineering, Proc. Inst. Mech. Eng. C 212 (8) (1998) 687–703.
[146] V. Chandola, A. Banerjee, V. Kumar, Anomaly detection: A survey, ACM Comput. Surv. 41 (3) (2009) 1–58.
[147] F. Magalhães, Á. Cunha, E. Caetano, R. Brincker, Damping estimation using free decays and ambient vibration tests, Mech. Syst. Signal Process. 24 (5) (2010) 1274–1290.
[148] E. Schlossmacher, An iterative technique for absolute deviations curve fitting, J. Amer. Statist. Assoc. 68 (344) (1973) 857–859.
[149] H.P. Gavin, The Levenberg-Marquardt Algorithm for Nonlinear Least Squares Curve-Fitting Problems, Vol. 3, Department of Civil and Environmental Engineering Duke University, 2019, August.
[150] P.C. Hansen, V. Pereyra, G. Scherer, Least Squares Data Fitting with Applications, JHU Press, 2013.
[151] S. Jacobsen, J.H. Mork, S.F. Lee, L. Haugan, Pumping of Concrete and Mortar-State of the Art, Tech. rep., SINTEF Building and Infrastructure, 2009.
[152] D. Kaplan, F. de Larrard, T. Sedran, Design of concrete pumping circuit, ACI Mater. J. 102 (2) (2005) 110, Copyright - Copyright American Concrete Institute Mar/Apr 2005; Document feature - Graphs; Illustrations; Equations; Diagrams; ; Last updated - 2023-11-17. URL https://proxy.lib.umich.edu/login?url=https://www.proquest.com/scholarly-journals/design-concrete-pumping-circuit/docview/197955281/se-2.
[153] H. Li, D. Sun, Z. Wang, F. Huang, Z. Yi, Z. Yang, Y. Zhang, A review on the pumping behavior of modern concrete, J. Adv. Concr. Technol. 18 (6) (2020) 352–363, http://dx.doi.org/10.3151/jact.18.352.
[154] J. Hu, Z. Ge, K. Wang, Influence of cement fineness and water-to-cement ratio on mortar early-age heat of hydration and set times, Constr. Build. Mater. 50 (2014) 657–663, http://dx.doi.org/10.1016/j.conbuildmat.2013.10.011, URL https://www.sciencedirect.com/science/article/pii/S0950061813009215.
[155] 3D concrete printing homes, 2025, https://usa.sika.com/en/construction/concrete/3d-concrete-printing/3d-concrete-printing–1k.html, (Accessed 23 March 2025).
[156] HS-40 colloidal silica Aldrich CAS No.7631-86-9 (principal component), 2025, https://www.sigmaaldrich.com/US/en/product/aldrich/420816?srsltid=AfmBOopF3_ONxQyxzR6Sg5Ur3IF8HpyHMWqbNebY2E6ZR_2g3YR0wWIH, (Accessed 23 March 2025).
[157] QUIKRETE Portland cement (no. 1124), 2025, https://www.quikrete.com/dealers/products/portlandcement.asp, (Accessed 23 March 2025).
[158] Boral, Boral Micron3, 2025, https://www.boralmti.com/pages/flyashtechdata.html, (Accessed 23 March 2025).
[159] QUIKRETE commercial grade sand (no. 1961–1963), 2025, https://www.quikrete.com/productlines/sandcommercialgrade.asp, (Accessed 23 March 2025).
[160] M.A. Haustein, M.N. Kluwe, R. Schwarze, Experimental investigation of the pumping of a model-concrete through pipes, Materials 13 (5) (2020) 1161, http://dx.doi.org/10.3390/ma13051161.
[161] Y. Ren, C. Bi, W. Lu, J. Zhi, W. Yang, J. Li, H. Wang, Research on nonconstant and discontinuous pumping characteristics of the concrete pump truck, Lubricants 11 (5) (2023) http://dx.doi.org/10.3390/lubricants11050217, URL https://www.mdpi.com/2075-4442/11/5/217.
[162] S. Vukosavic, M. Stojic, Suppression of torsional oscillations in a high-performance speed servo drive, IEEE Trans. Ind. Electron. 45 (1) (1998) 108–117, http://dx.doi.org/10.1109/41.661311.
[163] C.J. Watson, 2K robotic 3D concrete printing sensor dataset for process anomaly detection, 2025, http://dx.doi.org/10.5281/zenodo.17308420.